NUMERICAL STUDY OF SOLIDIFICATION AND THERMAL-MECHANICAL BEHAVIORS IN A CONTINUOUS CASTER

by

John Lawrence Resa

A Thesis

Submitted to the Faculty of Purdue University

In Partial Fulfillment of the Requirements for the degree of

Master of Science in Mechanical Engineering

Department of Mechanical and Civil Engineering

Hammond, Indiana

December 2020

THE PURDUE UNIVERSITY GRADUATE SCHOOL
STATEMENT OF COMMITTEE APPROVAL

Dr. Chenn Q. Zhou, Chair

Department of Mechanical and Civil Engineering

Dr. Harvey Abramowitz, Member

Department of Mechanical and Civil Engineering

Dr. Ran Zhou, Member

Department of Mechanical and Civil Engineering

Approved by:

Dr. Chenn Q. Zhou

I dedicate this thesis to the unmoved mover to whom all things are possible.

To my parents,

Thank you for all the support and love you gave me along the way.

To my friends,

Thank you for your companionship. The intimate conversations, comradery, banter and tomfoolery are all essential for a healthy, happy, and successful life.

I am proud to say that I am the average sum of my peers. May we all achieve greatness.

To myself,

Always take the road less traveled and bulldoze past obstacles that seem unfathomable. And for Christ sake, just do the thing you are supposed to do every day, and maybe, just maybe, you'll achieve your dreams. Be strong and wise, but don't forget to be compassionate.

ACKNOWLEDGMENTS

I would like to acknowledge the Steel Manufacturing Simulation and Visualization Consortium (SMSVC) members for supporting the research discussed in this study, and more specifically, the industrial collaborators (IC) who provided the geometry, operating conditions, validation data, and technical expertise for this study.

I would also like to acknowledge the Center for Innovation through Visualization and Simulation (CIVS) for providing the resources and environment to grow my knowledge exponentially with application driven research. A special thanks to my mentors, Dr. Armin Silaen, Matt Moore, and Haibo Ma for being exceptional in their leadership and understanding of the very interesting topic of steel. Also, a special thanks to my research team Edwin Mosquera, and Xiang Zhou, and all the rest of the CIVS family who helped me along the way.

Finally, I would like to thank my thesis advisory committee members: Dr. Chenn Zhou, Dr. Harvey Abramowitz, and Dr. Ran Zhou for generously offering their time, support, guidance, and goodwill throughout the preparation and review of this document.

.

TABLE OF CONTENTS

LIST OF TABLES

LIST OF FIGURES

LIST OF ABBREVIATIONS

BC	Boundary Conditions
BF	Broad Face
BSM	Breakout Shell Measurements
CC	Continuous Casting
CFD	Computational Fluid Dynamics
CIVS	Center for Innovation through Visualization and Simulation
CKMZ	Carman-Kozeny Mushy Zone
CMP	Constant Material Properties
F&S	Flow and Solidification
FEA	Finite Element Analysis
FVM	Finite Volume Method
HCS	High Carbon Steel
HF	Heat Flux
HT	Heat Transfer
IC	Industrial Collaborators
LCS	Low Carbon Steel
MCS	Mid Carbon Steel
MP	Material properties
MZ	Mushy Zone
NF	Narrow Face
PC	Primary Cooling
PDAS	Primary Dendrite Arm Spacing
PP	Perfectly-plastic
SC	Secondary Cooling
SEN	Submerged Entry Nozzle
SMSVC	Steel Manufacturing Simulation and Visualization Consortium
SP	Savage-Pritchard
SS	Steady-state
TD	Temperature Dependent

TDMP	Temperature Dependent Material Properties
UD	User Defined
UDF	User Defined Function
ULCS	Ultra Low Carbon Steel
UTN	Upper Tundish Nozzle
VP	Visco-plastic

NOMENCLATURE

a	Savage-Pritchard Peak Heat Flux Coefficient
A	Cross-Sectional Area
A	Crystal Characteristics Parameter
A_{inlet}	Cross-Sectional Area of Domain Inlet
A_{outlet}	Cross-Sectional Area of Domain Outlet
α	Thermal Expansion Coefficient
α^*	Model Coefficient
b	Savage-Pritchard Heat Flux Depreciation Coefficient
b_{force}	Total Body Force
c	Shape Factor for Dendritic Growth
D	Tangent Modulus
δ	Power-Regression Predicted Shell Thickness Profile
E	Elastic Modulus
ε_{creep}	Creep Strain
ε_{el}	Elastic Strain
ε_{flow}	Flow Strain
ε_{pl}	Plastic Strain
ε_{th}	Thermal Strain
F	Non-Dimensional Switching Function
f_{β^*}	Free-Shear Modification Factor
f_{cr}	Critical Relative Solid Volume Fraction
f_s	Relative Solid Volume Fraction
$\boldsymbol{g}$	Gravity
h	Enthalpy of the Liquid-Solid Phase
h_s	Sensible Heat
k	Turbulence Kinetic Energy
k_0	Ambient Turbulence Value
L	Latent Heat of Fusion

λ_1	Primary Dendrite Arm-Spacing
η	Scaling Factor for The Heat Flux Profile in the Mold Corners
p	Pressure
ρ	Density
ρ_{inlet}	Density of Steel at Inlet
ρ_{tc}	Density of Steel at Torch Cutoff
$\dot{q}_{Actual}$	Heat Transfer Rate Indicated from the Mold Surface Measurement Data
$\bar{q}''_{Msrd}$	Average Surface Heat Flux Determined from Measurement Data
$\dot{q}_{Tot}$	Total Heat Transfer Rate through a Mold Surface
$\dot{q}_{corner}$	Scaled Heat Transfer Rate in the Corner Regions of the Mold Surface
$\dot{q}_{std}$	Heat Transfer Rate from the Standard Heat Flux Profile
$\mathbf{q}''$	Heat Flux Vector
q''_{BF}	Heat Flux Profile Defined for the Broad Face Boundary Conditions
q''_{NF}	Heat Flux Profile Defined for the Narrow Face Boundary Condition
q''	Mold Heat Flux Profile
S	Energy Source per Unit Volume
σ	Stress
$\nabla\sigma$	Cauchy Stress
σ_k	Model Value
T	Temperature
t	Time
T^*	Normalized Temperature
T_l	Liquid Temperature
T_{ref}	Reference Temperature
T_s	Solid Temperature
$\vec{U}_{pull}$	Casting Velocity Vector
$\vec{U}$	Velocity Vector
u_{cs}	Casting Speed

u_{inlet}	Inlet Velocity
μ_l	Dynamic Viscosity of the Liquid
μ_t	Turbulent Eddy Viscosity
μ	Viscosity
$\dot{V}_{steel}$	Volumetric Flow Rate of Steel
w	Horizontal Offset from the Center of the Mold Surface
ΔW_{corner}	Mold Corner-Offset Distance for Decreased Heat Flux
ΔW_{std}	Width of the Mold Surface between the Corner Offsets
ΔW	Working Width of the Mold Surface
ω_0	Ambient Turbulence Value
ω	Specific Dissipation Rate
y	Depth below the Meniscus
ΔY	Working Height of the Mold Surface

ABSTRACT

Solidification and stress numerical models were developed in order to predict flow, shell thickness, and deformation of the shell within the mold. An investigation of temperature dependent material properties (TDMP) determined that temperature dependent (TD) viscosity has the most significant impact on flow and solidification (F&S). A steady-state (SS) F&S model validated simulated results to be within 8% of breakout shell measurements (BSM) provided by an industrial collaborator (IC). A transient F&S case replicating the casting speed and superheat change that occurred before the breakout condition was validated to be within 10% of BSM. A carbon percentage F&S investigation of 4 steels showed that shell growth increased with lower carbon percentages primarily because of changes in mushy zone (MZ) range and TD viscosity. A 2D simplification presented by Koric and Thomas for shell thickness and stress was validated to be within 1%, and 13%, respectively. The newly validated perfectly-plastic (PP) and visco-plastic (VP) stress-strain relations were then applied to a 3D portion of the shell within the mold to analyze stress and deformation. The VP model in comparison to the PP model showed higher amounts of stress but lower amounts of displacement because of the incorporation of more realistic flow and creep strains. The shell at lower casting speeds contracts more inwards because of bending stresses therefore producing larger air gap formation. Lastly, deformation within the shell of the 4 carbon percentage solidification study were compared, and results showed a (Narrow-Face) NF taper ranging from 2mm to 5mm.

1. INTRODUCTION

1.1 Continuous Casting Overview

Continuous casting (CC) is the most utilized steel making process today, making over 90% of the world's steel [1]. The CC process can be broken down into two cooling processes, primary cooling (PC) and secondary cooling (SC). First, raw or scrap steel is heated within a furnace until it is liquid, and then it is transported with a ladle into the tundish. The tundish regulates flow through the Upper Tundish Nozzle (UTN) into the Submerged Entry Nozzle (SEN) using either a stopper rod or slide gate. The SEN can also regulate flow into the mold using a slide gate. Once the melt reaches the convection cooled copper mold, PC begins as the melt solidifies and forms a shell around the molten core. The solidifying steel is then pulled by rollers into the SC zone, where the steel is further cooled and solidified using spray nozzles that intermittently spritz the solidifying shell with water between the rollers. Once the steel is completely solidified it is cut using a flame torch, and later refined into billets, slabs, or blooms [2]. Figure 1.1 depicts the main processes and features within CC.

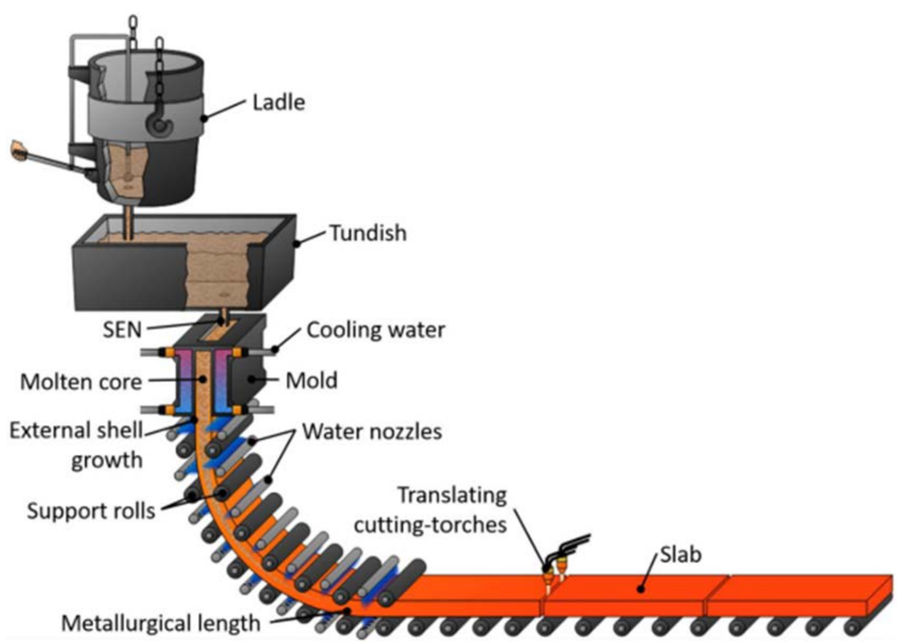

Figure 1.1 Continuous caster overview [3].

The PC zone of CC instigates solidification and is the most important cooling portion because a shell most be formed rapidly in order to contain the molten steel core. If cooling in the mold is inadequate, then defects and even breakouts are prone to occur. A breakout is when the molten core escapes through the thin shell which results in a loss of thousands of dollars due to equipment damage and downtime. Additionally, a breakout can potentially lead to extreme worker injuries and even death. The breakout shell can be carefully extracted from the mold and used for solidification model validation. Heat transfer (HT) from the mold is controlled by convection of the superheat from the jet to the shell front, conduction through the solidified shell, conduction from the mold wall through the flux lubricant to the solidifying steel, and convection from the cooling waterways in the mold. The biggest HT is from the mold wall to the molten steel [4].

Breakouts essentially occur from over cooling or under cooling from the mold to the shell. A hot and deep penetrating jet can lead to shell thinning at the impingement zone along the narrow face (NF). The mold cannot cool the shell quick enough and ultimately ferrostatic pressure will force the molten steel to burst through the thin shell. Lubrication is also vital in reducing breakouts and preserving high steel quality. Improper lubrication can lead to overcooling and the shell sticking to the mold wall. A “sticker” can lead to cracks, irregular depressions, and tearing of the shell. The tearing of the shell almost always leads to a breakout occurrence.

Most quality defects originate from complex flow phenomena therefore it is required that casting operations are constantly regulated in order to maintain high steel quality. For example, a cool meniscus can lead to hook formation which increases the likelihood of particle and argon bubble entrapment which substantially decreases steel quality. One could decrease the submergence depth of the SEN to negate the hook formation by melting it with the superheat coming from the jet, but this could also lead to an unstable meniscus. An unstable meniscus can cause level fluctuations which can entrap the slag layer that sits on top. This slag entrainment is also detrimental to the steel quality, so a healthy balance of heat and flow distribution is needed. The introduction of stabilizing argon gas and optimizing casting operations by thorough investigation from CFD modeling and experimentation can help reduce some of these flow related defects. It is important to optimize the casting operations in the PC zone because it is the last place in which the steel can be refined before it becomes completely solidified [5].

Other works describe these complex phenomena in greater detail and can be found elsewhere [2], [5], [6]. Figure 1.2 clearly depicts a few of the many complex phenomena that occurs within the CC process. This work will mainly focus on the solidification and stress in the PC zone.

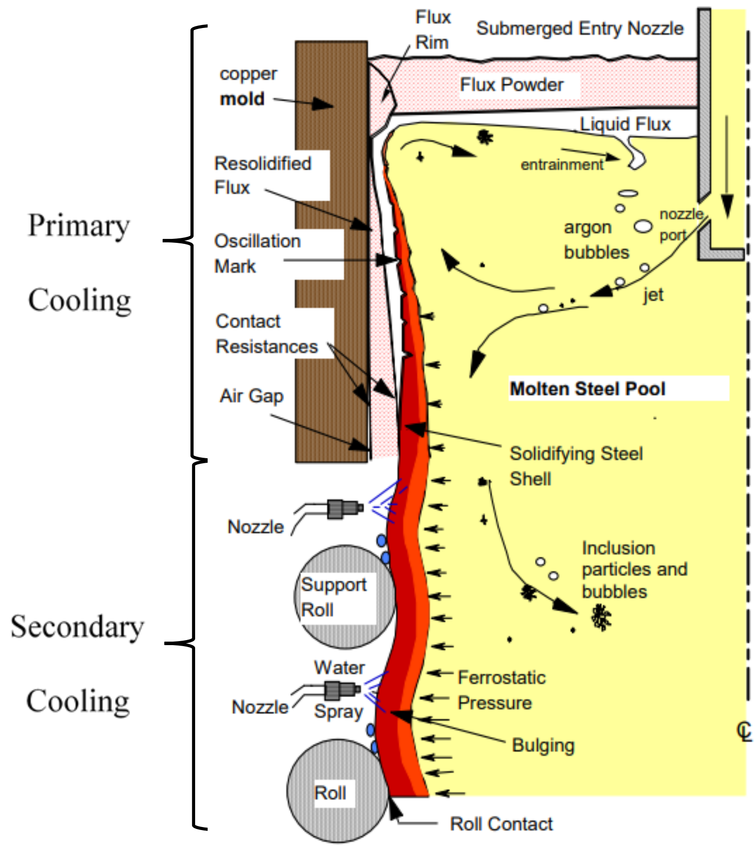

Figure 1.2 Primary and secondary cooling physical phenomena [6].

1.2 Motivations and Objectives

CC has advanced considerably with the help of 21st century technology. Many operations are well maintained and optimized with high temperature enduring equipment that will give a good indicator of irregular cooling and a warning system for a breakout. Although CC has made significant strides, problems originating from PC and SC have substantial impact on internal and external defects that results in significant losses in quality. A majority of these issues originate from the solidification front and the many complex phenomena that occurs close to it as shown in Figure 1.2. CC is intrinsically dangerous because of the high temperatures associated with the casting of molten steel. Plant based experiments are often expensive, impractical, and limited because of the dangerous temperatures. CFD and FEA offers an alternative solution to these risk by providing insights to these complex phenomena with the use of physics applied simulations. When simulating CFD and FEA models one often has to sacrifice accuracy and complexity for practicality and computational time. The primary focus of this paper is to develop accurate and computationally inexpensive solidification and stress models that are application driven to increase steel quality and reduce breakout occurrences for our IC.

The primary goal for both of these models are to make them as accurate as possible in order to predict real life casting phenomena. The goals of the F&S model were to firstly, determine the necessary TDMP required for an accurate model by using an iterative method. The professional thermo-data software, JMAT-Pro, was used to obtain the TDMP. The final results from the TDMP investigation were used to validate with BSM. The next goal was to expand on this SS F&S model by replicating the transient casting conditions provided by an IC from the sticker alarm up until the moment of the breakout. The purpose of simulating both was to gain a better understanding of time dependent BC and compare the results. After shell growth was validated with BSM, a parametric study on flow and shell growth for four different carbon percentages was conducted to understand its impact for IC.

With the advancement of the solidification model and the ability to obtain thermal-mechanical properties from JMAT-Pro, an advanced thermal-mechanical stress model could be created. Validation for a thermal-mechanical stress model in the shell within the mold is more difficult because of the inherently high temperatures and constantly moving components. Therefore, PP and VP stress relations for a solidifying body were validated and then applied to the shell within the mold. Thermal-mechanical research of a solidifying body for a 3D body within the mold is limited, therefore pseudo-validation comparing temperature and stress distribution within a 3D quarter portion of the shell was related with Koric and Thomas's work in Abaqus. Three different 3D quarter shell cases were created to compare the two different stress relations and two different casting speeds. Lastly, the 3D quarter shell was taken from the four carbon percentage investigation cases and deformation was analyzed in each. The ultimate goal of the stress model is to provide suggestions such as mold taper design or cooling suggestions to improve steel quality.

1.3 Simulation Software

When simulating solidification, mesh sensitivity and control is essential in order to validate the results with BSM accurately. Developing an in-house code to determine F&S within a caster would be labor intensive because of the complex nature and physics of solidification. Therefore, a commercial CFD software such as ANSYS, Star-CCM+, and COMSOL would be more optimal. Ultimately, the finite volume method (FVM) commercial software, Star-CCM+, was the best option because of its advanced solidification modeler and superior mesh options. In order to remain consistent with software and simplify the methodology, Star-CCM+'s FEA model was used to simulate the thermal-mechanical behaviors in the shell as well.

2. LITERATURE REVIEW

The following literature review section presents former research related to F&S and thermal-mechanical modeling. There are a few numerical methods for modeling solidification within the mold, and shell thickness can be validated by measuring the thickness at different locations of breakout shells. The enthalpy-porosity method for modeling solidification has been proven to be effective and accurate in other works [7], [8]. Thermal-mechanical stress research hasn't been as extensive because validation is difficult because of the dangerously high temperatures of solidifying steel, and difficult BCs the mold presents to the shell because of phenomena such as air gap [9], [10]. Brian Thomas is the most predominant researcher of CC and many of his works are used as the base of most modern day CFD and FEA casting models. Analyzing and incorporating the works of Thomas and other leading research groups are essential when creating a fully complex and comprehensive solidification and stress model.

2.1 Flow and Solidification Model

F&S coupled models have been successfully modeled in the past [8]. Others have opted to use 1D simplifications for solidification without the coupling of flow for the sake of computational expense [11]. Coupled F&S models may be more computationally expensive but offer greater detail to the shell growth that an uncoupled 1D model, such as the jet's impact on shell growth.

In order to imitate the cooling effects from the copper mold a cooling BC must be applied to each of the mold walls. The Savage-Pritchard (SP) heat flux (HF) approximation offers a simplified method for accurately imitating this cooling effect and has been successfully implemented in previously validated models [12]-[16]. It lacks in complexity and treats cooling as constant through the width of the surface. Other models have included the more accurate but computationally expensive HT modelling of the copper mold [17]. In this work the SP method is used to replicate the mold cooling effects. An interesting phenomena that needs to be accounted for within the heat flux profile (HFP) simplification is the air gap formation in the corners of the mold due to thermal shrinkage of the shell [9], [10]. The air gap decreases the cooling rate because the shell fails to make complete contact with the cooling mold wall. Brian Thomas offers a scaling factor solution to decrease the magnitude of the HF in these corner regions where the air gap forms [12].

The most dominant physical phenomena on flow and HT is the MZ region which is the zone between the liquidus and solidus temperatures. Columnar solidified dendrites forming along the shell front brake off from cross flow and slow the flow in the MZ region. The slower and thicker moving molten steel consequently impacts the conductive and convective HT and therefore the shell growth. Carman and Kozeny introduced a MZ model which relates the microstructure of the dendrites with its larger impacts on flow and HT [18], [19].

Proper mesh refinement is needed to accurately simulate a coupled F&S model. Special attention is needed where the jet impinges on the NF because of high temperature gradients from the rapidly cooling steel. Also the refinement within the potential shell front must be small enough to accurately simulate the shell thickness for validation with BSM [8]. The sensitivity of these measurements needs to be within the millimeter in order to get proper validation so the cell count can be substantial for these coupled models.

2.2 Thermal-Mechanical Stress Model

There are many mechanical moving components within the CC process such as the oscillating mold, solidifying shell, and rollers that pull the shell. With all these processes each item must endure the effects of thermal-mechanical fatigue. This work will focus particularly on the complex thermal-mechanical behaviors of the solidifying shell. It is disposed to a variety of distortion, cracking, and segregation because of high temperature gradients through the shell thickness, unique plastic deformation because of the inherently high temperatures, and intricate physical interaction with the mold and rollers. The high temperature gradient produces thermal distortion and shrinkage because of bending stresses. The high temperatures create unique plastic creep strain. The constitutive relation must be a function of temperature as the stress-strain characteristics change as temperature changes accordingly to the mechanical-properties of the material.

Weiner and Boley provide a baseline semi-analytical solution for a PP constitutive relation for stress in a solidifying body [20]. They treat the constitutive relation for stress-strain as a function of temperature. However, this work oversimplifies the plastic deformation region by treating stress as constant past the yield point. A more complex constitutive stress relation is needed in order to represent the distinguishing plastic creep and flow strains found in solidifying bodies. S. Koric and B.G Thomas validate and expand on this semi-analytical approach with CON2D; treating the solidifying body with a VP constitutive relation [21]. There are several other works that utilize a variation and expansion of Weiner and Boley's semi-analytical approach for solid stress numerical models [21]-[29].

The applications of these stress relations are often simplified to a 1D or 2D slice with assumed plane stress because of the 3D model's computational inefficiency and sophisticated BC. Brian Thomas's undergrad group has used this 1D simplification with CON1D to develop NF mold taper design suggestions for a Nucor Steel thin slab caster [24]. B.G. Thomas and others have also used a 2D simplification with CON2D to investigate mold corner radii and air gap formation in billet casters [10], [25]. There are also several other areas of focus including hook formation [27], [28], and mold distortion [12]. Zapulla recently simulated the full solidifying shell length within a continuous caster, however it was with a course mesh because of the large geometry [26]. S. Koric and B.G. Thomas apply the VP stress relation to a 3D quarter section of the shell within the mold using Abaqus, and incorporate the effects of fluid flow and TDMP [29]. A similar quarter shell geometry is used within this work to investigate the effects of stress and deformation in the shell within the mold at different casting speeds and with different steel compositions.

3. METHODS

The work presented in this research is a part of a larger ongoing project focused on developing a comprehensive numerical model for a CC. All the models that are created are application driven to improve steel quality and limit breakouts for IC. This particular section will explain the methodology used to develop the models, and the physics that went into each of the models.

3.1 Model Development Methodology

Due to the complexity of CC modeling, the comprehensive model for PC was broken down into several subcomponents in order to properly manage each of the physical phenomena. The TD SS F&S model was built on a former constant material property (CMP) SS F&S model. The CMP SS F&S model was built on former isothermal single phase and multiphase (molten steel and argon gas) models. The transient F&S model added complexity to the SS model with transient BCs. Advancements with thermo-data software JMAT-Pro and shell growth results from the validated TD F&S model led to the thermal-mechanical stress model. Figure 3.1 shows this macro scale methodology.

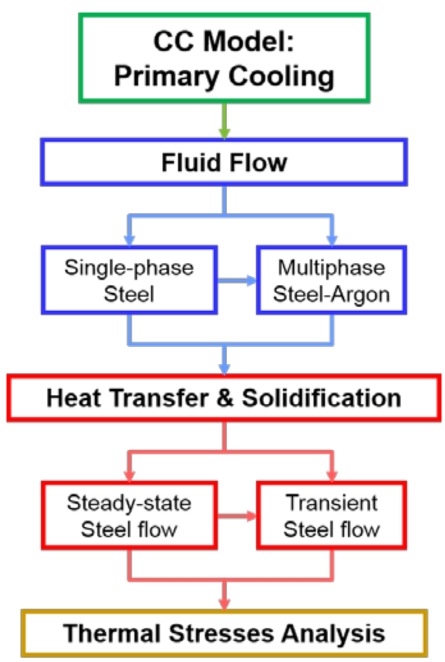

Figure 3.1 Methodology used for the development of the CC model.

The methodology for this particular study starts with distinguishing which TD properties are needed and which can be discarded in the validation of the SS F&S model. Once the SS F&S model was complete, the transient F&S model was created with variable BC replicating the effects of a breakout condition. The flow and shell growth were analyzed through time and the results were validated at the time of the breakout. With a well validated solidification model the next step was developing the thermal-mechanical stress model.

First, the model was validated using the simplified PP stress-strain relation. It was applied to a quarter of the shell and compared to a similar case presented by Koric and Thomas to ensure the model was going in the right direction. The PP relation was then applied to half the shell to analyze the deformation of the shell within the mold. Next, the more advanced VP stress relation with the more realistic creep and flow strains was validated. The VP stress relation with TDMP was applied to a quarter of the shell for two different casting speeds from the transient solidification case, 40ipm and 20ipm. An additional case with a PP relation and TDMP was compared to the VP case at 40IPM. Lastly, a parametric study on 4 carbon percentages took place to investigate the effects on F&S, and deformation. Figure 3.2 shows an overview of the methodology explained above.

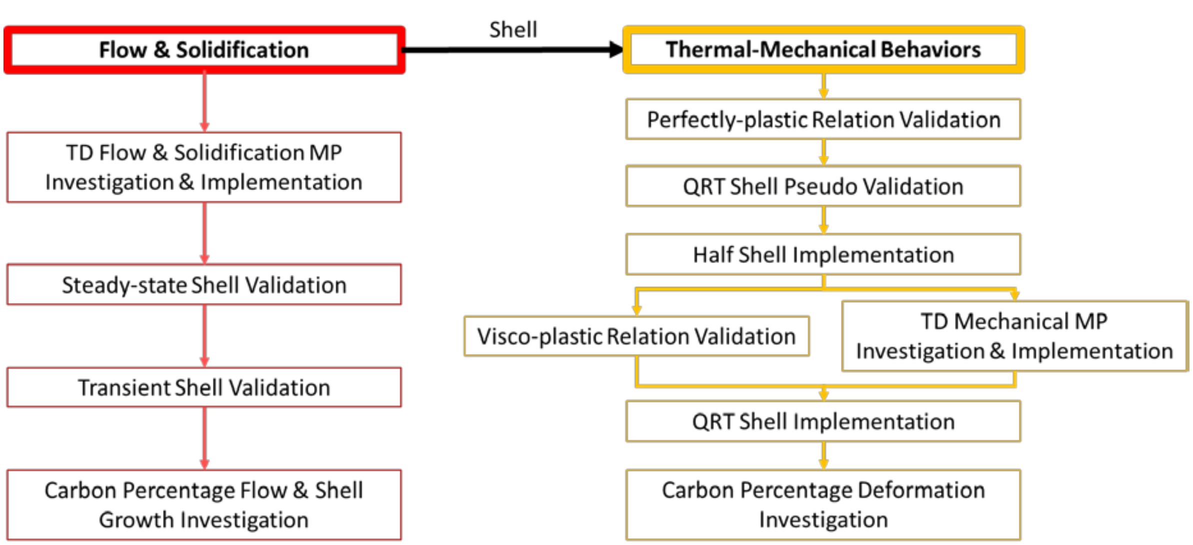

Figure 3.2 Methodology used in this work.

3.2 Flow and Solidification

The flow model evaluates turbulence using the Reynold Average Navier Stokes (RANS) k-ω shear stress transport (k-ω SST) model. This model incorporates good features from both the standard k-ω model and k-ε model. The k-ω SST allows for better treatment of boundaries such as walls or baffles compared to the standard k-ω model with the use of blending functions, and also predicts flows with separation and adverse pressure gradients better in comparison to the k-ε model [30]. The turbulent kinetic energy, k, and the specific dissipation rate, ω, are obtained from the following transport equations.

$$\frac{\partial}{\partial t}(\rho k) + \nabla \cdot (\rho k \vec{\mathrm{u}}) = \nabla \cdot [(\mu + \sigma_k \mu_t)\nabla k] + P_k - \rho \beta^* f_{\beta^*}(\omega k - \omega_0 k_0) \qquad (3.1)$$

$$\frac{\partial}{\partial t}(\rho \omega) + \nabla \cdot (\rho \omega \vec{\mathrm{u}}) = \nabla \cdot [(\mu + \sigma_\omega \mu_t)\nabla \omega] + P_\omega - \rho \beta f_\beta(\omega^2 - \omega_0^2) \qquad (3.2)$$

Where the turbulent viscosity, μ_t, is calculated as follows:

$$\mu_t = \rho k \alpha^* / \omega \qquad (3.3)$$

Flow resistance due to solidification is calculated using the enthalpy-porosity method which utilizes a momentum source term dependent on a switching function to replicate the effects of the MZ and solidified shell. The first zone governed by the Metzner Slurry Viscosity Model represents low solid fraction areas, and assumes the primary phase of the solid-liquid mixture to be molten steel, where the presence of small solidified crystals within the melt are responsible for an increasing viscosity [18]. The second zone governed by the Carman-Kozeny Mushy Zone (CKMZ) permeability model treats the viscosity in a sudden manner as it assumes dendritic crystal growth advancing towards the melt to be the root of increased flow resistance [19]. This work only utilizes the CKMZ model.

Momentum equation with resistance source term:

$$\frac{\partial}{\partial t}(\rho \vec{\mathrm{u}}) + \nabla \cdot (\rho \vec{\mathrm{u}} \times \vec{\mathrm{u}}) = \rho \vec{g} + \nabla p + \nabla(\mu \nabla \cdot \vec{\mathrm{u}}) + S \qquad (3.4)$$

Where the Metzner Slurry effective viscosity, μ, is calculated as follows:

$$\mu = \mu_l [1 - \left(\frac{\boldsymbol{F} f_s}{A}\right)]^{-2} \qquad (3.5)$$

And the Carman-Kozeny momentum resistance source term, S, is solved as follows:

$$S = -\mu\left(\vec{\mathrm{u}} - \vec{\mathrm{u}}_{pull}\right) F \left(\frac{{f_s}^2}{(1 - f_s)^3}\right)\left(\frac{c}{\lambda^2}\right) \qquad (3.6)$$

Where the switching function, F, is represented by:

$$F = \begin{cases} 0.5 - \dfrac{\arctan[f_s - f_{cr}]}{\pi} & for\ slurry\ region \\ 0.5 + \dfrac{\arctan[f_s - f_{cr}]}{\pi} & for\ porous\ region \end{cases} \tag{3.7}$$

The variable c is the Carmen-Kozeny shape constant which is taken as 1645 based on Pfeiler's work [8]. The variable λ represents primary dendrite arm spacing (PDAS) and was taken as $1.24*10^{-4}$ m based on B.G Thomas and D. Stone's research [31]. The volume fraction approach for solidification is represented in Figure 3.3; one can see the 3 defined regions within the model for liquid, MZ, and solid.

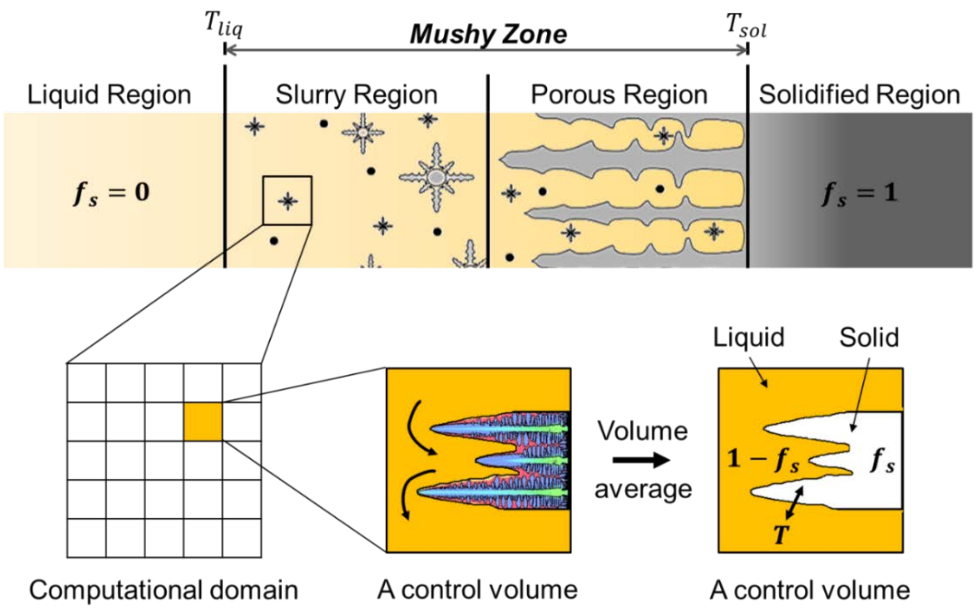

Figure 3.3 Volume fraction solidification approach.

Energy or enthalpy is evaluated with a piecewise function based on the relative solid volume fraction. The enthalpy will change the HT properties depending on the region being simulated (the solidified shell, MZ, or molten steel).

$$\frac{\partial}{\partial t}(\rho h) + \nabla \cdot (\rho h \vec{u}) = \nabla \cdot (\alpha \nabla T) + L \frac{\partial}{\partial t}(\rho f_s) + \rho L \vec{u}_{pull} \cdot \nabla f_s \tag{3.8}$$

Where the enthalpy of the liquid-solid phase, h, is calculated as follows:

$$h = h_s + L(1 - f_s) \tag{3.9}$$

The relative solid volume fraction is TD, and a piecewise function is utilized to correct the enthalpy of the liquid-solid phase. Further details on the Enthalpy-Porosity model can be found elsewhere [32].

$$f_s = \begin{cases} 1 & \text{if} \quad T^* < 0 \\ 1 - T^* & \text{if} \quad 0 < T^* < 1 \\ 0 & \text{if} \quad 1 < T^* \end{cases} \tag{3.10}$$

Where the normalized temperature, T^*, is defined as follows:

$$T^* = \frac{T - T_s}{T_l - T_s} \tag{3.11}$$

3.2.1 Coupling Fluid Flow and Solidification

When conducting former CMP solidifcation simulation it was noted that flow was significantly dampened because of the MZ and default critical solid fraction (CSF) of 0.27. In order to adjust for this excessive dampening of the flow, a new method for flow dampening and solidification is created by allowing TD total viscosity to govern most of the flow. When utilizing the CKMZ model it is traditional to use a constant or TD dynamic viscosity. To clarify dynamic visocity is the visocity for moving fluid which does not include the added effects of flow resistance when steel solidifies, while total visocity includes this added resistance.

The advantage of governing the flow with total visocity rather than a combination of dynamic viscoisty and added dampening from porous visocous resistance is that total viscosity represents the dampening of the flow more accurately. Many added assumptions and variables such as PDAS, and shape constant are needed in order to use a method like the CKMZ model which can drastically add to the discrepancies in flow.

The method used in this work is an adaptation of the CKMZ model, which moves the CSF from 0.525 for traditional 0.2% carbon steel to 0.95 and silumtaneously using a TD table for total viscosity. This allows the total viscosity to govern a majority of the flow while allowing the dampening and stopage of the flow to be governed by the MZ model. This model is an improvement over using the traditional CKMZ method with CSF = 0.525 in regards to flow, however it is not perfect because excessive flow dampening is still added.

3.2.2 Shell Growth Validation

The shell thickness measurements were taken from a segment of the shell located at the quarter width of the mold (half distance from the SEN to the NF). The segment was approximately 100 mm wide, and about 1 m in height. The segment was measured at 5 mm intervals along both sides, extending from the thin portion located near the meniscus towards roughly 0.1 m below the mold outlet. The IC noted that approximately the top 3 inches (76.2 mm) of the recovered shell segment had broken off during the recovery process. Also, it was suggested that only the top portion of the shell should be used for validation because it took more time for the molten core to drain downstream. The results were validated by comparing the BSM from this recovered shell segment with simulated results within the F&S model. For visual purposes one can view the location and measurements of the shell in Figure 3.4.

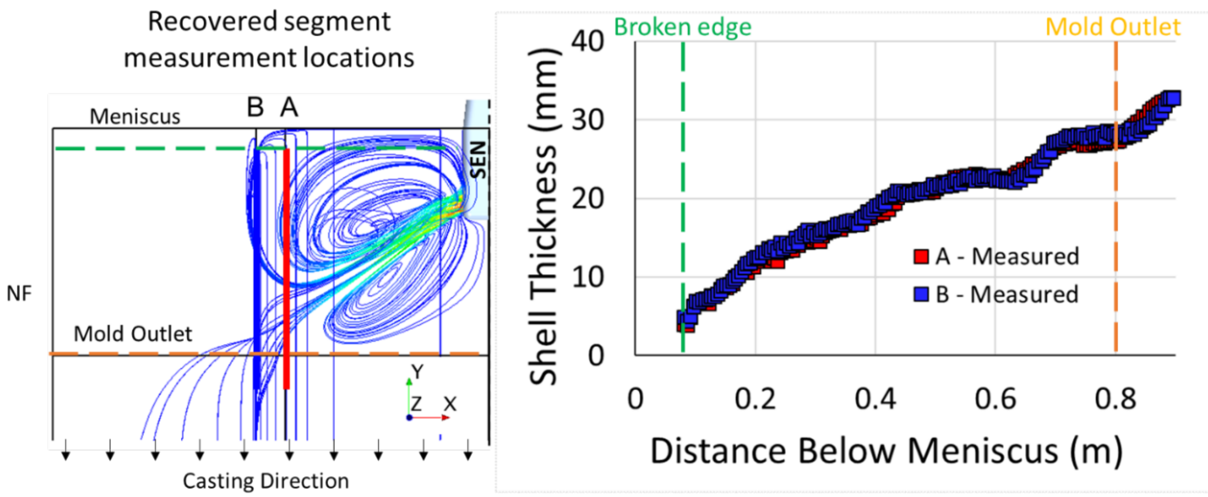

Figure 3.4 Recovered shell thickness locations and measurements.

3.2.3 Variable Casting Conditions Effects

SS simulations are computationally inexpensive, but do not always represent the actual casting operations. Therefore, a transient simulation with variable BCs for casting speed and superheat was created to represent breakout conditions more accurately. The numerical procedure involves a two-stage process, first a SS simulation is conducted to obtain the shell thickness at normal casting operations, and then a transient simulation is used to replicate the breakout condition recorded by an IC. An illustration of this process can be visualized in Figure 3.5. The potential of this transient BC simulation is not only accurate and real time shell thickness but also real time stress and deformation as described in Figure 3.6.

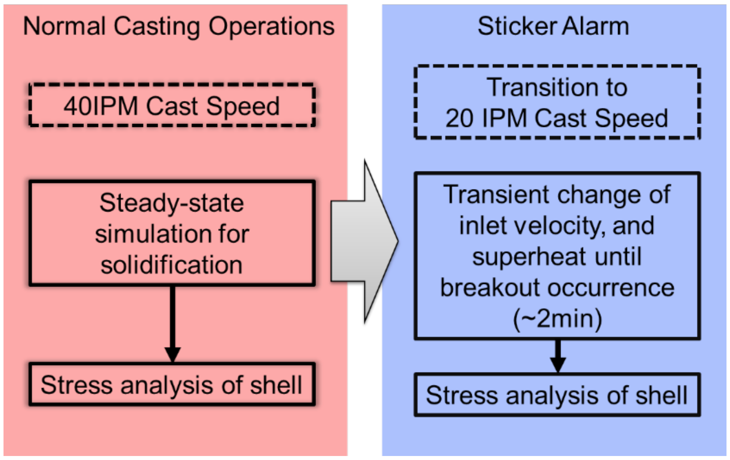

Figure 3.5 Transient solidification model methodology.

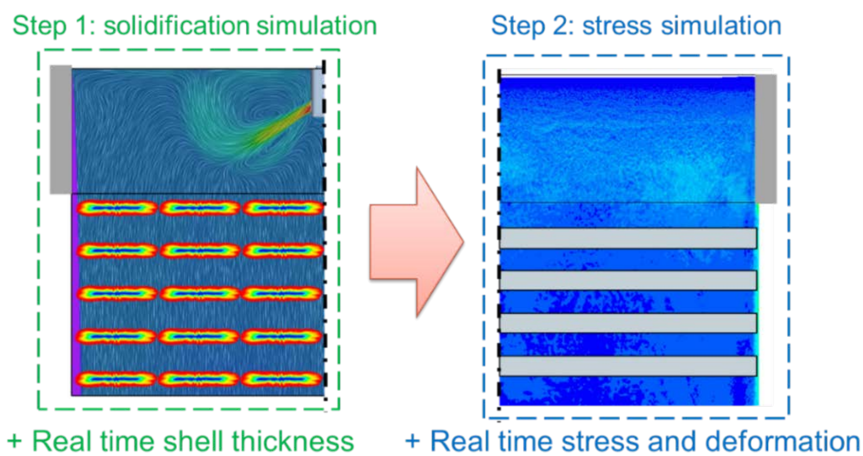

Figure 3.6 Transient solidification model benefits.

3.3 Thermal-Mechanical Stress

A finite element method (FEM) approach is utilized to solve for stress, strain, and displacement. Thermal-mechanical behaviors in the shell are calculated by two constitutive stress-stress relations. These models must assume relatively small strains in order to avoid divergence due to drastic changes within the material which would lead to cracking. In general, stress at any point within the model can be defined by a second-order tensor of the following form [33]:

$$\sigma = \begin{pmatrix} \sigma_{xx} & \sigma_{xy} & \sigma_{xz} \\ \sigma_{yx} & \sigma_{yy} & \sigma_{yz} \\ \sigma_{zx} & \sigma_{zy} & \sigma_{zz} \end{pmatrix} \tag{3.12}$$

Where stress and strain have the following constitutive relation:

$$\sigma = D(\varepsilon_{total} - \varepsilon_{th} - \varepsilon_{pl} - \varepsilon_{flow} - \varepsilon_{creep}) \tag{3.13}$$

Where ε_{pl} is plastic strain, ε_{creep} is creep strain, ε_{th} is thermal strain, and ε_{flow} is flow strain. D is the slope of the stress-strain curve at any specific stress or strain or the material tangent modulus. All mechanical properties are assumed to be uniform or isotropic throughout the shell for simplicity. For an isotropic material, the thermal strain is described as:

$$\varepsilon_{th} = \alpha(T - T_{ref}) \tag{3.14}$$

Where α is the thermal linear expansion coefficient, and T_{ref} is the reference temperature, where strain is assumed to be 0.

Each of the strains add a layer of both complexity and accuracy to the model. The first validated constitutive relation is the thermo-elastic-perfectly-plastic or constitutive stress-strain relation or PP for short. This model simplifies the inelastic region by assuming constant stress past the yield point. It is better than a simple elastic or thermo-elastic model but lacks the unique plastic behavior a solidifying body exhibit. Therefore, the thermo-elastic-visco-plastic constitutive stress-strain relation or VP was developed and validated. All these constitutive relations are described in eqns. (3.15)-(3.18).

Elastic model	$\sigma = E\varepsilon_{el}$	(3.15)
Thermo-elastic model	$\sigma = D(\varepsilon_{total} - \varepsilon_{th})$	(3.16)
Thermo-elastic-perfect-plastic model	$\sigma = D(\varepsilon_{total} - \varepsilon_{plas} - \varepsilon_{th})$	(3.17)
Thermo-elastic-visco-plastic model	$\sigma = D(\varepsilon_{total} - \varepsilon_{th} - \varepsilon_{pl} - \varepsilon_{flow} - \varepsilon_{creep})$	(3.18)

Where E is the elastic modulus and ε_{el} is the elastic strain..

The motion and displacement of the solid is governed by Cauchy's equilibrium equation, which describes the conservation of linear momentum or movement for a given continuum:

$$\nabla\sigma + b_{force} = 0 \tag{3.19}$$

Where $\nabla\sigma$ is the Cauchy stress tensor and b_{force} is the total body force per unit volume.

3.4 Obtaining Temperature Dependent Properties from JMAT-Pro

The material properties (MP) for the F&S model and thermal-mechanical model are obtained through the professional thermo-data software, JMAT-Pro. The software allows one to enter three inputs, alloy composition, cooling rate, and grain size, to obtain the constant and TDMP needed for the models. The default grain size value of 500µm was used, and a 0.005°C/s cooling rate was used as suggested by an IC. The procedure for obtaining these MP is depicted in Figure 3.7. JMAT-Pro was utilized to obtain the MP for all the cases in this study besides the stress validation cases which were obtained through literature, and the quarter shell pseudo-stress-validation and half shell stress simulation cases which were obtained partially through online MP databases.

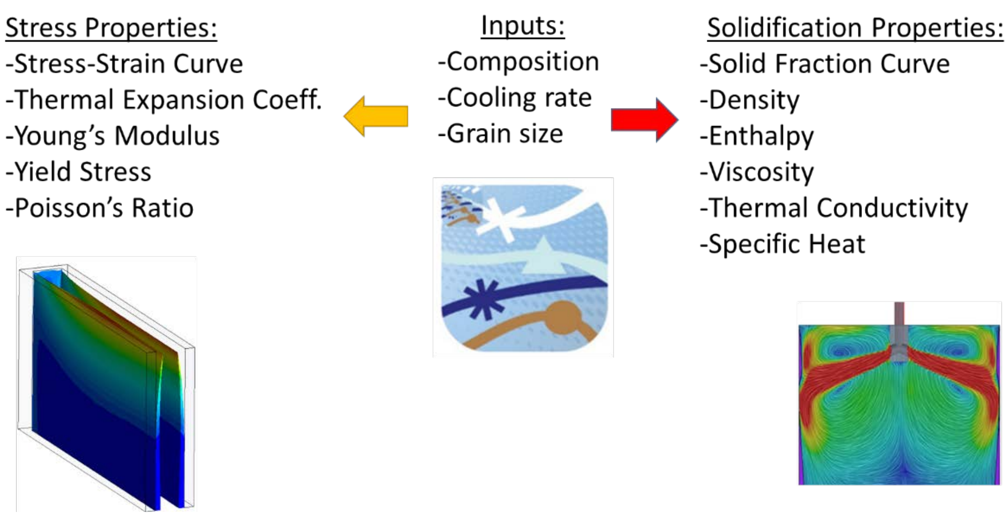

Figure 3.7 JMAT-Pro MP methodology.

4. GEOMETRY, MESH, AND BOUNDARY CONDITIONS

In this section the computational domains, mesh methods, and BCs will be presented for the F&S, and thermal-mechanical stress models. The stress validation geometry, mesh, and BCs are all mentioned in the results section. The domain used to validate the stress relations are small and can be briefly explained along with the BCs and results.

4.1 Computational Domain and Mesh

4.1.1 Flow and Solidification

A 3D simulation geometry was constructed based on a thin slab caster from an IC. The caster utilizes a stopper-rod for flow control, however, as the simulations conducted for this caster were primarily focused towards the development of the solidification model, the inlet geometry was simplified by neglecting the influences of the stopper-rod and UTN on the flow field and assuming a uniform velocity field across the inlet of the SEN. The domain was further simplified by the assumption that the influences of cross-flow and energy transfer between the two ends of the mold could be neglected, and that the flow field to either side of the SEN would be symmetric; thereby, allowing for the simulation to be performed using a half-mold domain. The general mold dimensions are provided in Table 4.1, and in Figure 4.1. The preliminary solidification domain began with the 3m domain length, but a parametric study showed that a 2.1m domain was sufficient. All simulations used in this study used the 2.1m domain, the 3m domain was shown as a reference.

Table 4.1 F&S casting parameters.

Dimension	Value
Mold width (half)	60.75 in (1.5431 m)
Mold thickness	6 in (0.1524 m)
Working mold height	31.5 in (0.8 m)

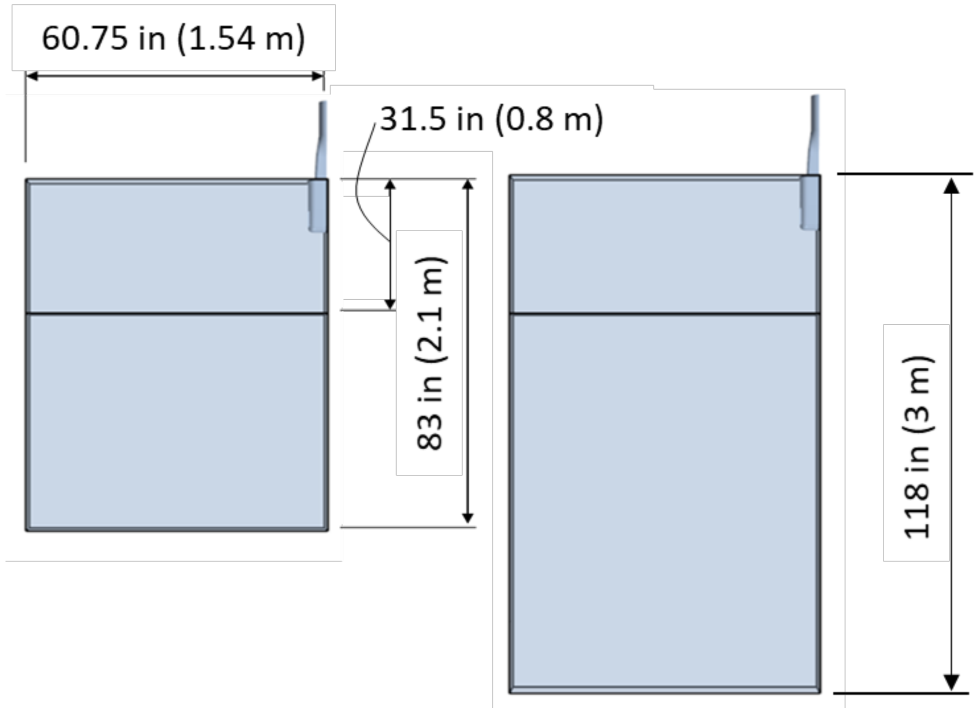

Figure 4.1 F&S caster computational domain.

The mesh for the solidification model uses a standard base size of 5mm in the mold and 10mm below the mold exit. A fine mesh refinement is needed to accurately obtain the shell thickness due to the high temperature gradient. The refinement zones for this shell growth were based on the obtained shell thickness measurements. The shell thickness measurements only extended to roughly 1 m below the meniscus and therefore an interpolated function for this shell growth was used to define are refinement zones. The shell growth followed a general trend of power regression of the following form with an R^2 value of 0.97:

$$\delta = 0.3035y^{0.6841} \tag{4.1}$$

5 mm of thickness was added to this general equation to allow for overgrowth and to not contain the shell growth in order to influence the validation results. Therefore, the final form for this relation of local refinement is defined as:

$$\delta = 5 + 0.3035y^{0.6841} \tag{4.2}$$

A section view of the mesh for the 3m domain is depicted in Figure 4.2. The mesh demonstrates similar characteristics for the 2.1m domain. One can see the described shell refinement zones and transition of core mesh size from PC to SC. The total cell count for the 2.1m domain was ~13 million.

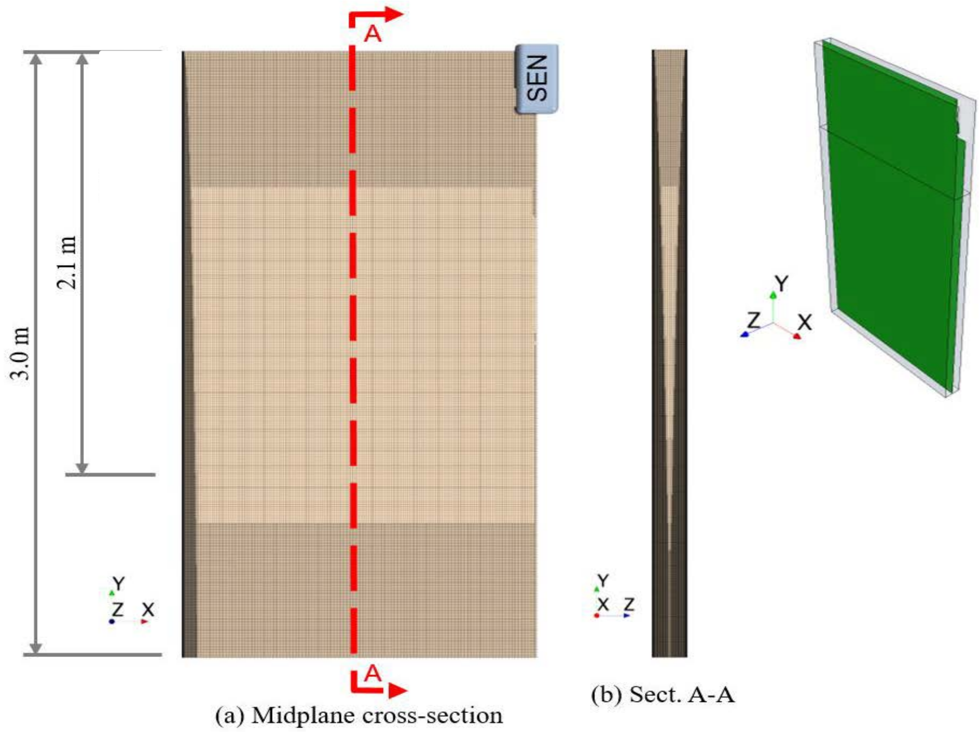

Figure 4.2 Dynamic shell front mesh: (a) midplane cross-section, and (b) A-A cross-section.

4.1.2 Thermal-Mechanical Stress

The 3D shell was extracted from the solidification model by creating an iso-surface for a solid fraction of 0.9 and extruding that outwards and intersecting it with the extents of the mold walls. The quarter shell came from the bottom quarter portion of the shell retrieved from F&S's breakout shell validation. The half shell and quarter shell are roughly 0.8m and 0.2m in height respectively. The total width is 1.54 m which matches the dimension constraints of the solidification domain, as represented in Figure 4.3. The base size for the mesh is 5mm which is based on BG Thomas's work [29]. A small 20mm refinement zone of 2mm base size is located in each of the NF corners because of the high temperature gradient that occur in each of the corners as shown in Figure 4.4. The total cell count for the quarter shell was ~400k for the 40IPM case and ~700k for the 20IPM case. The quarter shells alloy composition analysis simulations had ~500k cell count on average. The half shell simulations utilized a similar mesh shown in Figure 4.4 for two different simulation, one with a 10mm base size, and one with a 5mm base size. The half shell simulations for the 10mm base size and the 5mm base size had a total cell count of ~3 million and ~6 million, respectively.

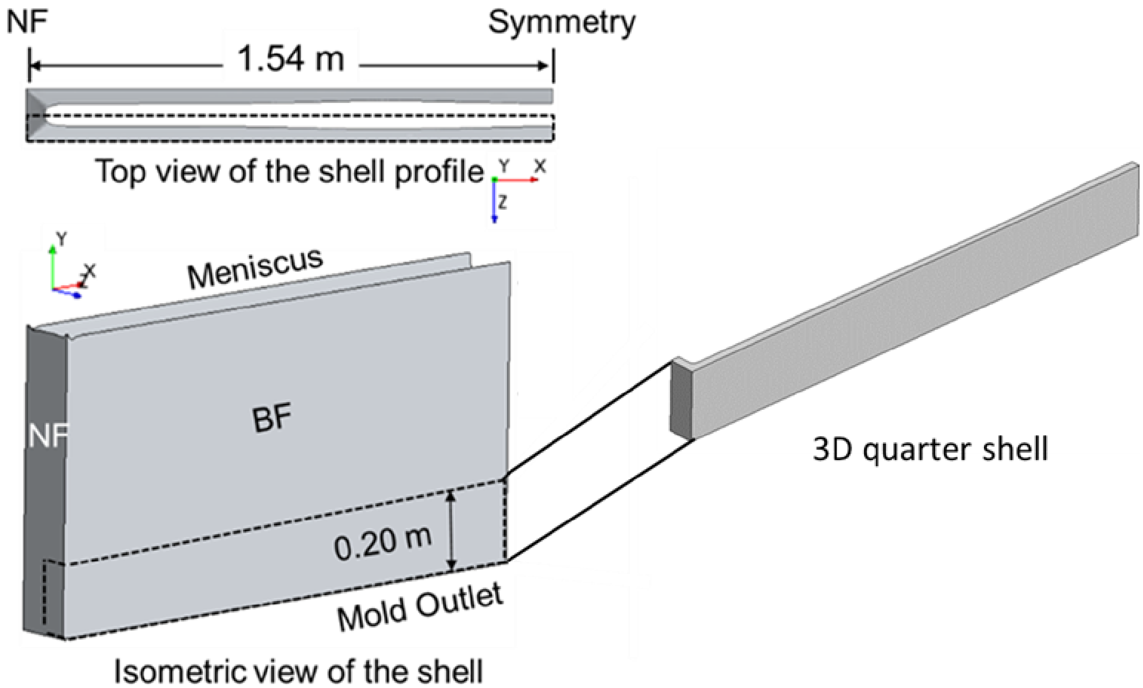

Figure 4.3 Stress 3D shell computational domain.

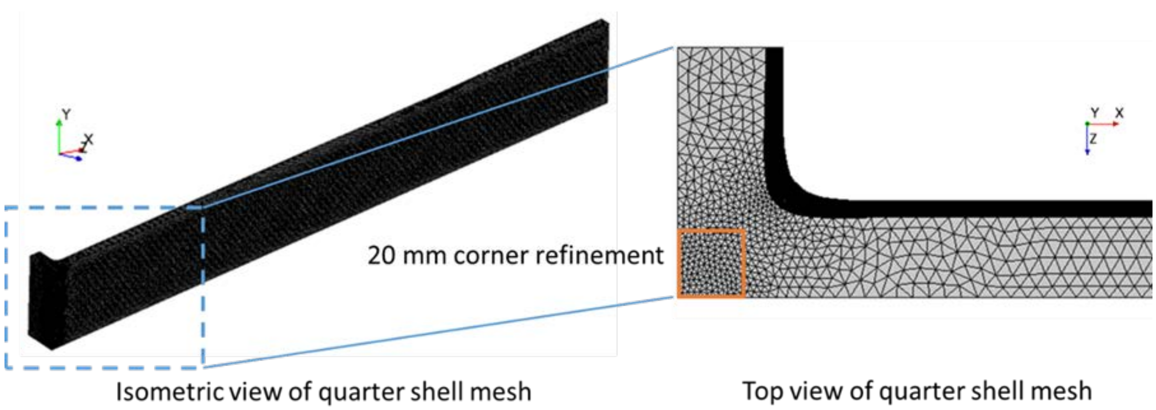

Figure 4.4 Mesh for 3D shell stress simulations.

4.2 Boundary Conditions and Material Properties

4.2.1 Flow and Solidification

Steady-state Boundary Conditions and Casting Parameters

Two primary SS F&S cases are presented in this work, one for shell thickness validation, and another for the carbon percentage parametric investigation. For the SS validation case casting operation data recorded by the IC up until the point of the breakout was used to determine the BCs for the inlet velocity, inlet temperature, casting speed, and cooling HFP within the mold. The SC data was considered proprietary at the time so an interpolated heat transfer coefficient (HTC) from literature was used in the SC region. A sticker alarm was noted ~143s before the breakout occurrence. 40s after the sticker alarm, the cast speed was reduced from 40ipm to 20ipm to encourage shell growth. The casting process continued for another ~60s before a new superheat was introduced, and a breakout occurred ~40s afterwards. The SS validation case replicated the casting operations provided by the IC ~40s before the breakout occurrence. The transient process is described in greater detail later in this section.

All of the SS carbon percentage investigation cases use the same standard casting operations. Table 4.2 presents the different casting parameter for all the SS simulations conducted in this study. The BCs used for the solidification model are found in Figure 4.5. As mentioned in section 4.1.1, half the geometry is used in order to save computational time and symmetry was applied across the center plane. There was many simplifications in order to reduce complexity such as: treating the meniscus as a slip wall, uniform flow through the SEN inlet, and interpolated boundary HFs.

Table 4.2 Casting parameters for solidification cases.

Case	Shell Thickness Validation	Standard Casting Operations
Submergence Depth	7.7 in (0.1956 m)	5.5 in (0.1397 m)
Casting Speed	20 IPM (0.5 mpm)	40 IPM (1 mpm)
Superheat	26 F (14.44 °C)	36 F (20 °C)

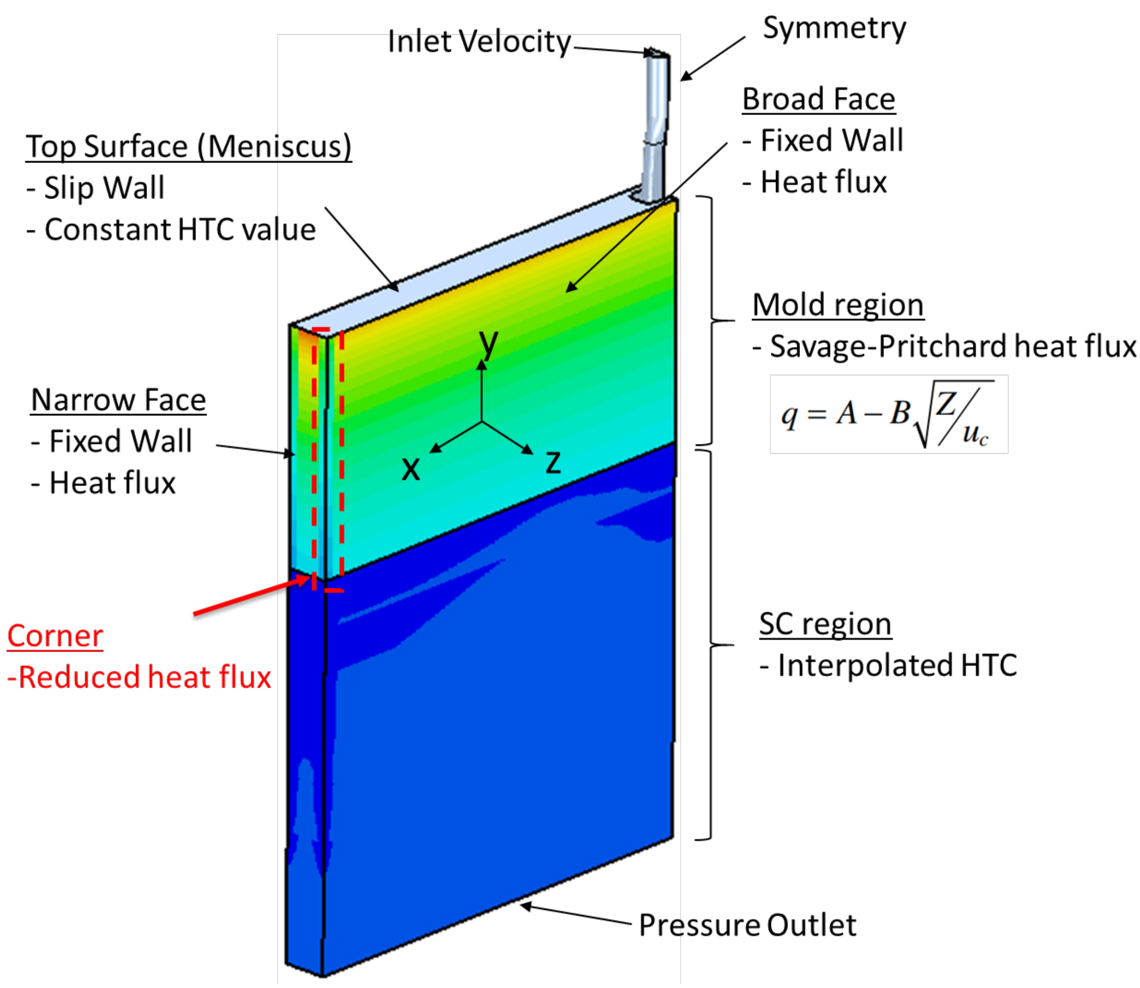

Figure 4.5 BCs for F&S model.

Conservation of mass and adjusting for change in density allowed for the inlet velocity to be approximated from the relation:

$$u_{inlet} = \frac{\rho_{tc}}{\rho_{inlet}} \cdot A_{inlet} \cdot \dot{V}_{steel} \tag{4.3}$$

Where ρ_{inlet} is the density taken at the temperature of the inlet, and ρ_{tc} is the density taken at the approximated torch cut off temperature of 1273K. The casting speed is represented as u_{inlet}, and the inlet and mold outlet cross sectional area are represented by A_{inlet} and A_{outlet}, respectively. $\dot{V}_{steel}$ represents the volumetric flow rate of steel through the domain, and is assumed as:

$$\dot{V}_{steel} \approx A_{outlet} \cdot u_{cs} \tag{4.4}$$

There are two sections in which the heat extraction must be interpolated on to the geometry, the PC zone and the SC zone. For the PC zone thermocouple and cooling water data was provided by an IC, and an average HF could be determined for the two broad faces (BF) and NF walls. However, it was determined that this would be insufficient because cooling from the mold tends to decrease from the meniscus downwards towards the mold outlet. As mentioned in section 2.1, the SP HF correlation can be used to approximate a fairly accurate HFP, and is represented as:

$$q''(y) \approx a - b\sqrt{\frac{|y|}{u_{cs}}} \tag{4.5}$$

where a represents the peak HF value at the meniscus, b is the HF depreciation coefficient, y denotes the vertical distance below the meniscus, and the casting speed is evaluated in units of meters-per-minute. The HFP is only a function of the vertical direction and therefore cannot account for change in the width directions and therefore is treated as constant for different values of y.

Thermal shrinkage, known to occur in solidifying bodies, reduces HT from the cool mold to the shell. The SP correlation was recognized by Gonzales et al. and others to create unrealistic temperatures in the corner regions of the shell if the SP was left unchanged [12]-[16]. In order to account for the HT reduction in the corners, Thomas et al. utilized a scaling factor that would decrease the cooling effects by 67% the standard value within 31mm from the mold corners [12]. The same approximation is used in this study for all F&S cases. This approximation is unlikely to be consistent for all cases because MP, shell thickness, and bending stresses will vary the air gap size. However, an iteration procedure is proposed for future simulation in section 5.3.2 to increase the accuracy of the cooling in these corner regions.

In order to simplify and assess the scaled down corner regions from the standard SP sections a relation was created for the working width of the mold and is defined as:

$$\Delta W = \Delta W_{std} + 2\Delta W_{corner} \tag{4.6}$$

where ΔW is the width of the working area for the considered surface, ΔW_{corner} represents the 31mm corner offset proposed by Thomas, and ΔW_{std} represents the width of the remaining surface where the standard SP HFP is applied.

After incorporating the scaling factor, the SP HFP could then be defined as:

$$q''(y) \approx \eta \left[a - b\sqrt{\frac{|y|}{u_{cs}}} \right] \tag{4.7}$$

where η is the HFP scaling-factor and defined as:

$$\eta(w) = \begin{cases} 1\,, & |w| < \left(\frac{\Delta W}{2} - \Delta W_{corner}\right) \\ \frac{2}{3}, & |w| \geq \left(\frac{\Delta W}{2} - \Delta W_{corner}\right) \end{cases} \tag{4.8}$$

where w represents the horizontal displacement from the surface center.

Two known conditions are needed to solve for the a and b coefficients in the SP HF relation. The average HF for each of the surfaces obtained through cooling data could be used but not directly. A comparison could be made between the measured and calculated values for the total heat transfer rate (HTR) for each surface. The actual HTR was assumed to be the product of the working surface area and the calculated average HF for that surface, and it is expressed as:

$$\dot{q}_{actual} = A \cdot \bar{q}''_{Msrd} = (\Delta Y\ \Delta W) \cdot \bar{q}''_{Msrd} \tag{4.9}$$

Where, $\dot{q}_{actual}$ is the actual HTR, $\bar{q}Msrd''$ is the average calculated HF from IC data for the given surface, ΔY is the height of the working surface area, A, of the considered BF or NF. The HFP was integrated over the working area of each BF and NF, to produce the following relation:

$$\dot{q}_{Tot} \approx \left(a \cdot \Delta Y - \frac{2}{3} b \sqrt{\frac{|\Delta Y|^3}{u_{cs}}} \right) \cdot \Delta W \tag{4.10}$$

Thomas noted in previous work that the HF value 25mm below the mold is approximately 70% greater than the average HF on that corresponding mold surface [34]. This allowed for the HF to be approximated at that single elevation of 25mm:

$$q''(0.025\ m) \approx 1.7\bar{q}''_{Msrd} \approx a - b\sqrt{\frac{(0.025\ [\mathrm{m}])}{u_{cs}}} \tag{4.11}$$

Where $\dot{q}_{Tot}$ is the total HTR of the surface and is defined as:

$$\dot{q}_{Tot} = \dot{q}_{std} + 2\dot{q}_{corner} \tag{4.12}$$

Where $\dot{q}_{std}$ and $\dot{q}_{corner}$ represent the HTR for the standard surface and HTR for the corners, respectively.

Eqn. (4.10) can also be represented by each of these HTR components separately:

$$\dot{q}_{std} = \left[\Delta Y\ a - \frac{2}{3} b \sqrt{\frac{|\Delta Y|^3}{u_{cs}}} \right] \cdot \Delta W_{std} \tag{4.13}$$

$$\dot{q}_{corner} = \frac{2}{3} \left[\Delta Y\ a - \frac{2}{3} b \sqrt{\frac{|\Delta Y|^3}{u_{cs}}} \right] \cdot \Delta W_{corner} \tag{4.14}$$

With eqns. (4.10) and (4.11) the SP coefficients, a and b, can be obtained by setting both equations equal to each other. The simplified relations are represented below:

$$a = \frac{\dot{q}_{std}}{|\Delta Y|\ \Delta W_{std}} + \frac{2}{3} b \sqrt{\frac{|\Delta Y|}{u_{cs}}} \tag{4.15}$$

$$b = \frac{0.7 \dot{q}_{std} \sqrt{u_{cs}}}{|\Delta Y|\ \Delta W_{std} \left[\frac{2}{3} \sqrt{|\Delta Y|} - \sqrt{(0.025\ [\mathrm{m}])} \right]} \tag{4.16}$$

After substituting known values into b, coefficient a can be solved and both can be plugged into eqn. (4.5) to get SP HFP relations for the BF and NF at a casting speed of 20ipm or 0.51mpm of the following form:

$$q''_{BF}(y) = 2.1 - 1.2 \sqrt{\frac{|y|}{0.51}} \tag{4.17}$$

And

$$q''_{NF}(y) = 2.6 - 1.5 \sqrt{\frac{|y|}{0.51}} \tag{4.18}$$

Where the results from eqns. (4.17) and (4.18) are in megawatts per meter squared. For visual purposes the calculated mold HF profiles for the BF and NF at the 20ipm casting speed are plotted in Figure 4.6.

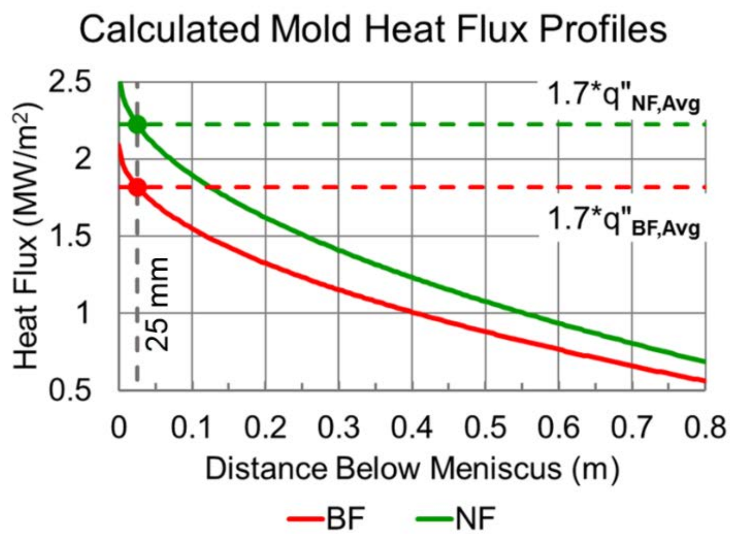

Figure 4.6 Derived HF profiles for the mold in the 20ipm solidification model simulation.

As mentioned previously, the SC zone was considered proprietary and therefore a simple vertical correlation was defined by using a HTC BC. This correlation was made rather than a constant value because of preliminary simulations and as per suggestion of IC. Meng and Thomas implemented this correlation which sums HT from convection, conduction, and radiation, over the SC surface area [11]. Using the literature, a profile for the HTC was derived from the SC parameters and the simulated surface temperature data. The separate cooling zones, the shell surface temperature, and locations of each nozzle and roll used in the evaluation of the HTC values, are plotted with the derived HTC profile in Figure 4.7.

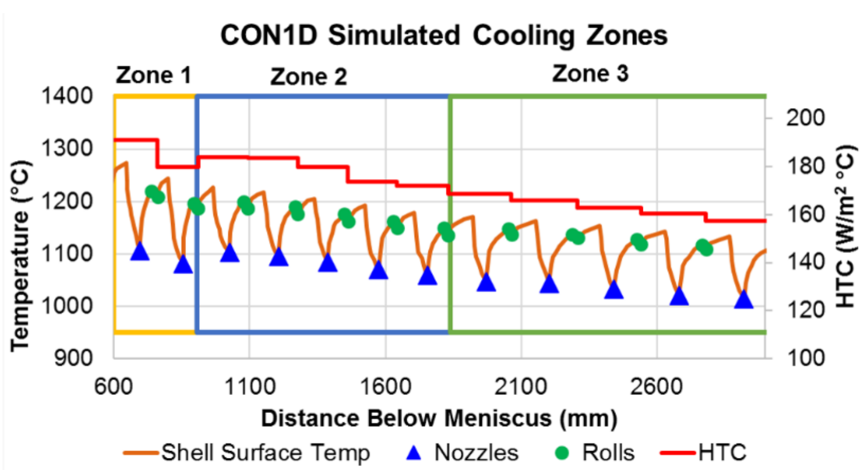

Figure 4.7 HTC values derived from the simulated surface temperature profile and nozzle-roll parameters from literature [11].

The HFP for the mold and the HTC correlation for the SC zone were applied using user-defined-functions (UDF) in Star-CCM+, they are depicted in Figure 4.8 (a). The resulting surface HF is shown in Figure 4.8 (b). All results shown in the derivation process for the solidification BCs are taken for the 20ipm cast speed. The same derivation process for the PC HFP and SC HTC was conducted for the 40ipm cast speed and applied to the corresponding cases.

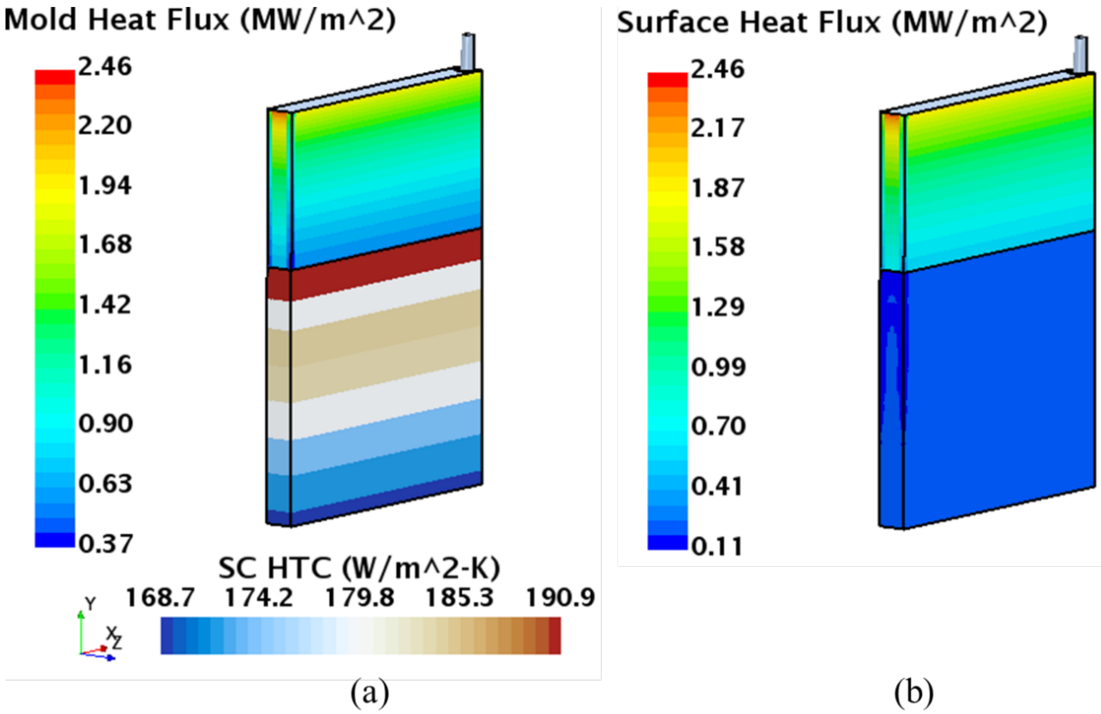

Figure 4.8 BF and NF surface contours depicting (a) the applied BC, and (b) the resulting surface HF at the 20ipm cast speed.

Breakout TD Material Properties

The TDMP used in the MP parametric investigation are displayed in Figure 4.9 to Figure 4.13. The CMP are plotted next to the TDMP in order to show the impact TDMP will have in comparison to their respective averaged out constant values. One can see that MP like thermal conductivity and density experience smaller changes from their constants in comparison to specific heat and viscosity.

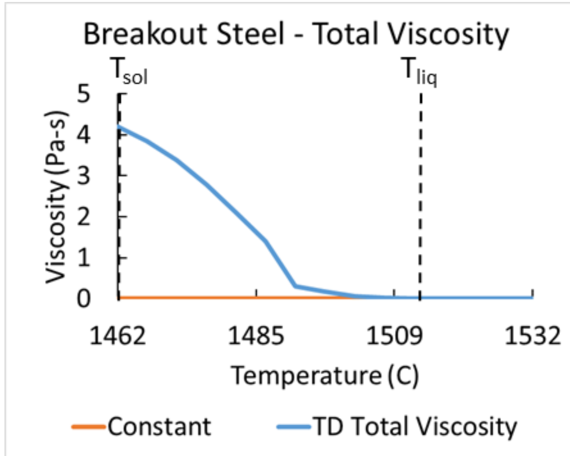

Figure 4.9 Breakout steel – TD total viscosity.

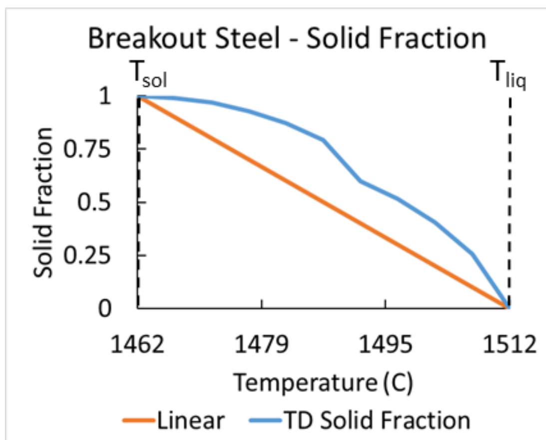

Figure 4.10 Breakout steel – TD solid fraction curve.

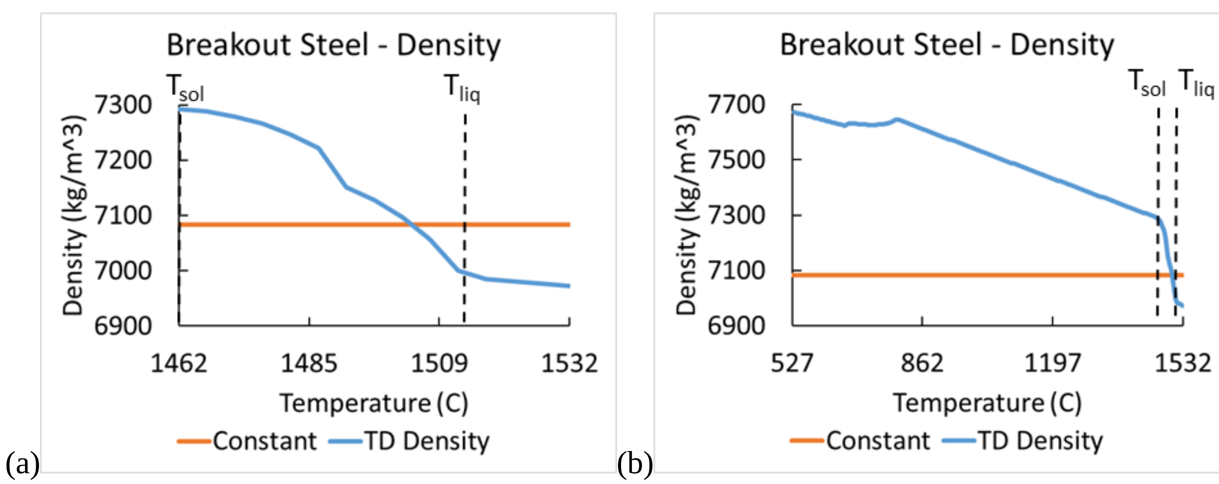

Figure 4.11 Breakout steel – TD density: (a) fluid region, and (b) solid & fluid region.

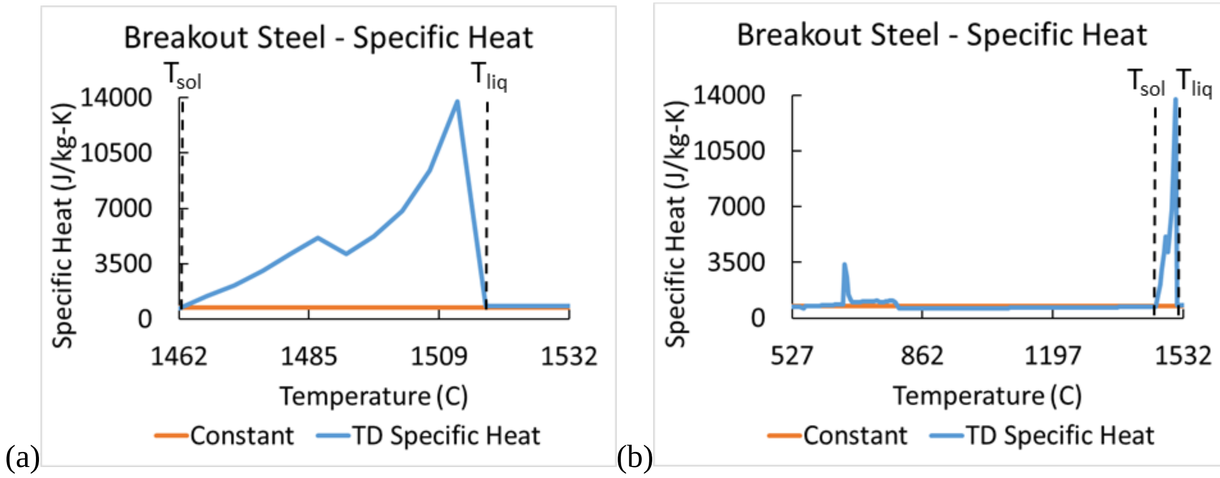

Figure 4.12 Breakout steel – TD specific heat: (a) fluid region, and (b) solid & fluid region.

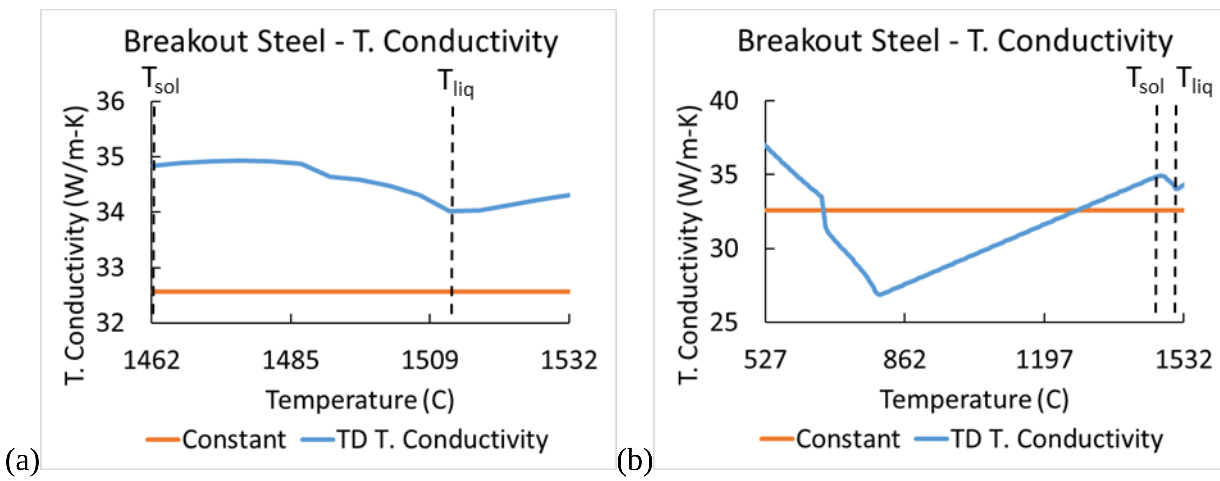

Figure 4.13 Breakout steel – TD thermal conductivity: (a) fluid region, and (b) solid & fluid region.

Variable Boundary Condition Effects

A sticker alarm happened 143s prior to the breakout occurrence. The first 40s after the sticker alarm the casting conditions stayed relatively the same as normal operating conditions so for the sake of computational time the first 40s was disregarded and a SS simulation was used to obtain the flow and shell thickness. The transient simulation begins 40s after the sticker alarm and the total simulation time is 103s. Two important changes are the casting speed transition from 41ipm to 20ipm (1mpm to 0.5mpm) from simulation time 40s to 45s, and the transition in superheat from 18 Δ°F to 26 Δ°F (10 Δ°C to 14.44 Δ°C) from 105s to 107s. A depiction of these variable casting conditions and events throughout time can be found in Figure 4.14.

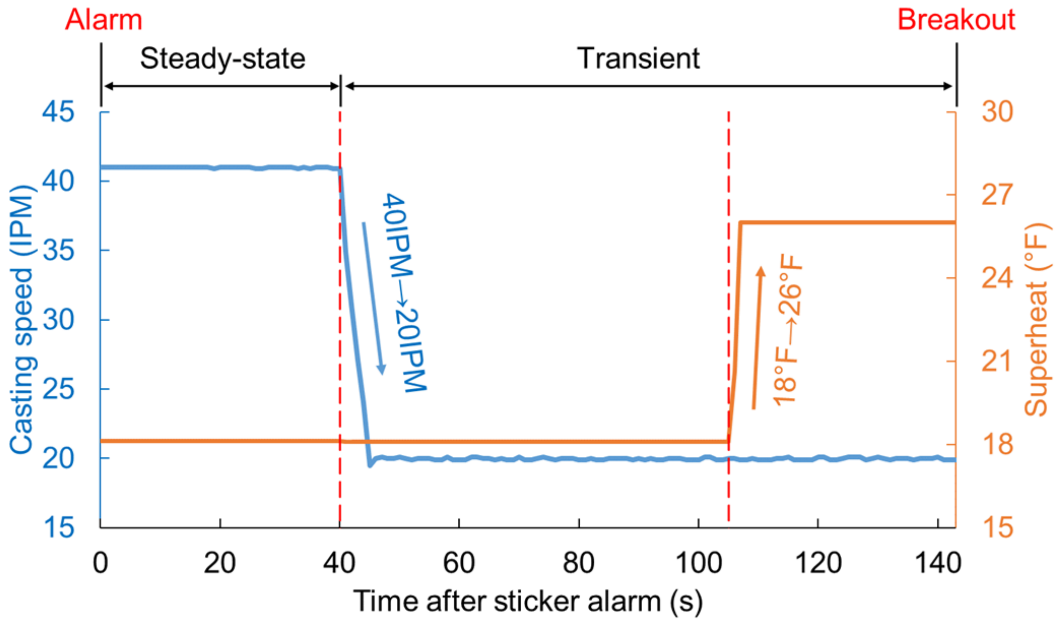

Figure 4.14 Transient solidification validation BCs.

Carbon Percentage Effects

The carbon percentage analysis has the same BC as the standard F&S model in the 40IPM case. The four steels that are being analyzed are ultra-low carbon steel (ULCS), low carbon steel (LCS), mid carbon steel (MCS), and high carbon steel (HCS). It is important to note that carbon percentage is not the only element percentage that is being changed, and therefore this is not a pure study on carbon percentage. A simplified breakdown of the compositions used is shown in Table 4.3. The MZ change (temperature difference between Liquidus and Solidus) in each of these steels vary as well as the TD-viscosity as displayed in Figure 4.15. Some of these alloys are proprietary so detailed information of the composition is not included.

Table 4.3 Compositions of steels used in alloy composition investigation.

Class	wt%Fe	wt%C	Other alloys
High carbon steel	80.73	0.87	18.4
Middle carbon steel	96.41	0.41	3.18
Low carbon steel	94.31	0.11	5.58
Ultra low carbon steel	97.89	0.05	2.06

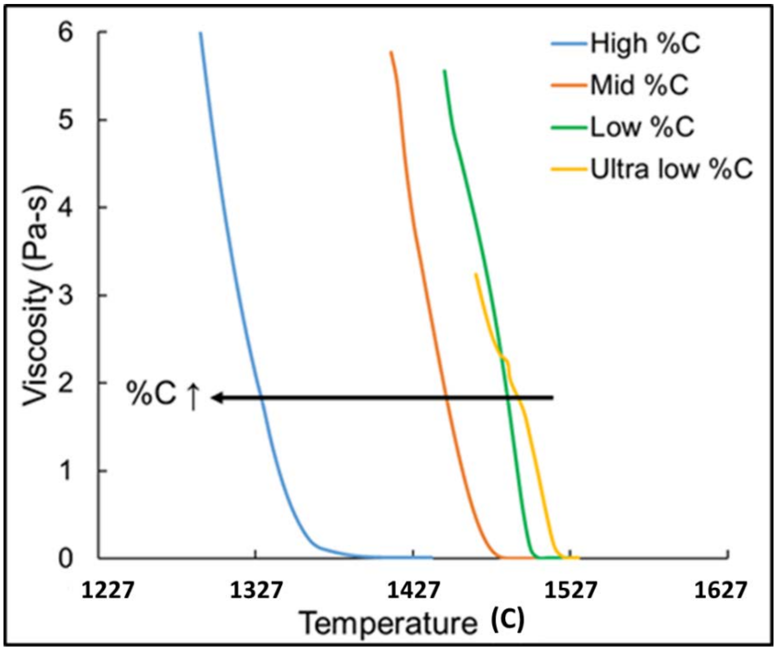

Figure 4.15 TD viscosity comparison plot.

4.2.2 Thermal-Mechanical Stress

3D Shell Boundary Conditions

A detailed diagram of the geometry and BC which were made to replicate that of BG Thomas's work is shown in Figure 4.16. Symmetry is applied to the top XZ plane surface, along the NF center XY plane surface, and at the YZ plane surface where the middle portion of the mold is located. Roller supports or zero vertical Y-displacement is applied at the bottom XZ plane surface where the mold exit is located. The temperature distribution is applied from the solidification cases using a xyz internal table to extract the temperature values within the solidified shell. A pressure BC is applied to the shell front to account for the ferrostatic pressure of the molten steel. Figure 4.17 shows both the applied temperature field and ferrostatic pressure. The BC for the half shell are similar to that of the quarter shell treating the mold outlet with a roller support and symmetry along the center YZ plane.

The most difficult BC to represent inside the simulation is the interaction between the mold and the shell because of complex physical phenomena that occurs when two bodies meet. In order to represent these interacting bodies a penalty enforcement BC was applied to the planes representing the BF and the NF. As the shell crosses past the BF or NF plane threshold, the method uses a penalty pressure of 1e11 Pa to force the shell back within the constraints of the mold. The 1e11 Pa value was based on the modulus of elasticity of steel. The penalty enforcement method is unstable in nature especially when using high values so a load stepping solver for external loads was used to increase the convergence of the simulations. The results using this method showed deflection to be less than 1mm outside the mold perimeters which is acceptable deformation at this depth within the mold.

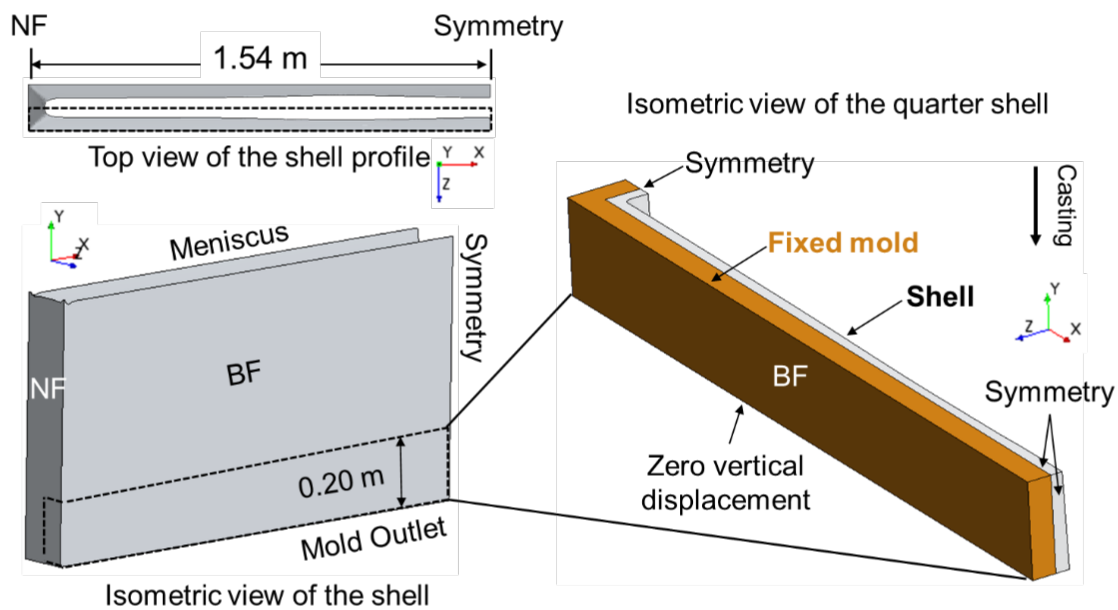

Figure 4.16 BCs for 3D quarter shell simulations.

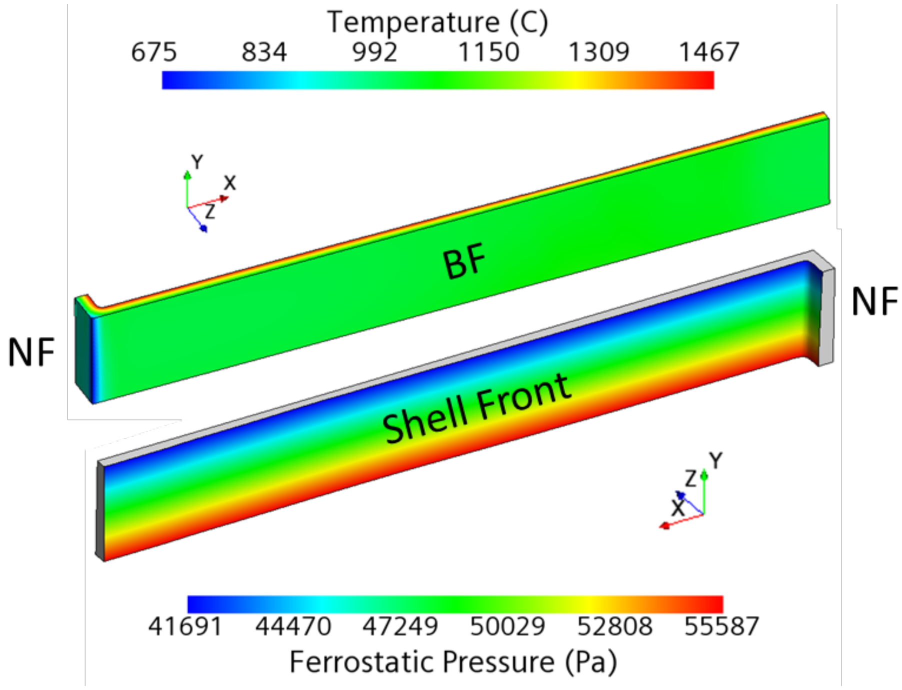

Figure 4.17 Temperature and ferrostatic contour plots on 3D quarter shell.

TD Thermal-mechanical Material Properties

A comparison of the PP stress-strain relation to the VP stress-strain relation can be found in Figure 4.18. One can see the underestimation of the stress in the plastic region when using the PP stress relation. The mechanical TDMP for the breakout steel are plotted against constant room temperature values, as shown in Figure 4.19 - Figure 4.21. The differences are drastic, and this emphasizes the importance of considering temperature's effect on not only solidification properties but also thermal-mechanical properties.

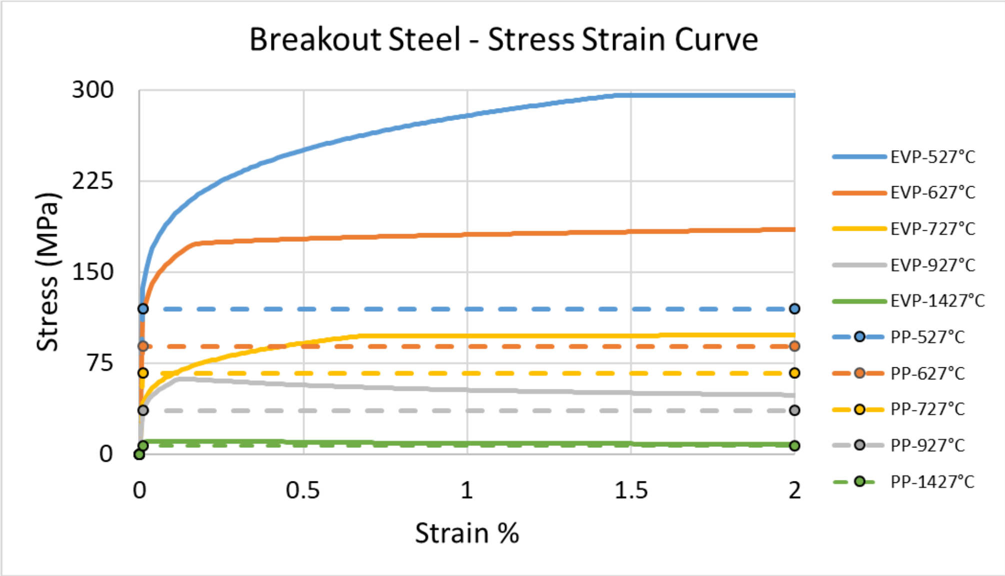

Figure 4.18 Breakout steel – TD stress-strain PP and VP comparison.

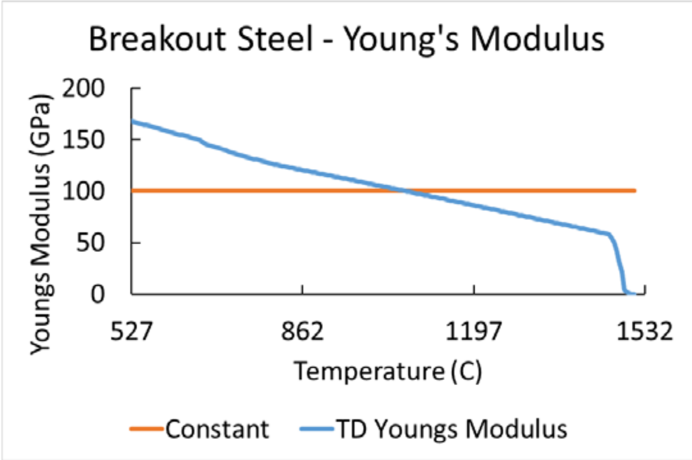

Figure 4.19 Breakout steel – TD Young's modulus.

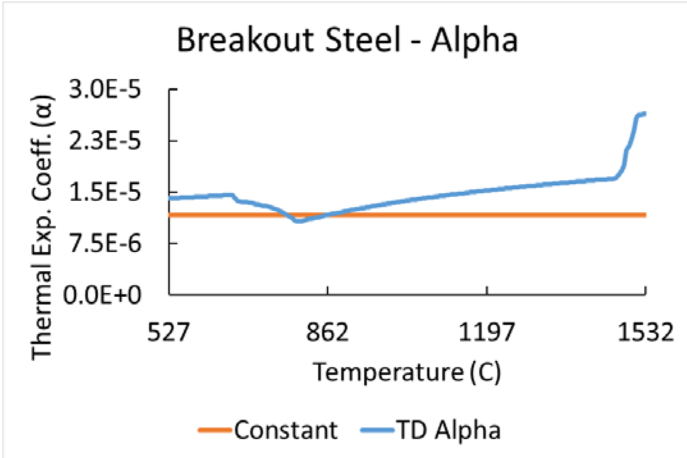

Figure 4.20 Breakout steel – TD thermal expansion coefficient.

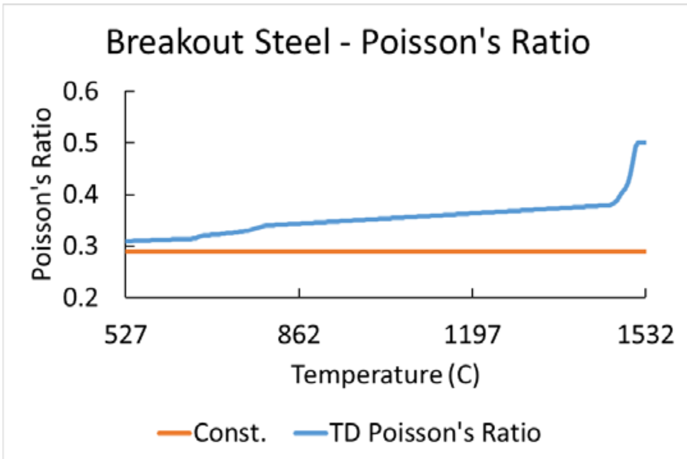

Figure 4.21 Breakout steel – TD Poisson's ratio.

5. RESULTS & DISCUSSION

In this section the results from this research will be presented in chronological order in which they were completed. The F&S results contain both a validation and applications. The applications of the F&S model are a transient boundary condition study and a carbon percentage investigation. The thermal-mechanical model starts with the validation and application of the PP model. Next, the more realistic VP relation is validated and applied to the shell. Lastly, the VP model is applied in a carbon percentage investigation for deformation.

5.1 Flow and Solidification

5.1.1 Solidification Validation

Temperature dependent material property investigation

In Star-CCM+ there are six MP inputs: solid fraction curve, density, enthalpy, viscosity, thermal conductivity and an option to use either specific heat or enthalpy. An analysis of these MP was performed in order to determine their impact and accuracy on shell growth as well as flow. An implementation procedure was developed to determine whether the TDMP should be incorporated into the model or discarded, it takes into account both significance and accuracy and is shown in Figure 5.1. Two iterations of this procedure were conducted and the results of each can be found in Table 5.1 and Table 5.2.

The parametric study shows that thermal conductivity, and density have little impact on the flow and shell growth. TD enthalpy/specific heat created irregular flow patterns and a severe undergrowth of the shell, so it was concluded that the solidification model within star added additional enthalpy. TD solid fraction did increase shell growth in comparison to the linear solid fraction relation but was not significant enough to add and was discarded to save computational time. TD viscosity at a CSF of 0.95 had the largest impact on the flow and shell growth as it exhibited the most ideal flow roll patterns and penetration, and the shell growth was closest to the BSM. Flow and shell thickness contours, and shell thickness measurement comparison plots for the first iteration are shown in Figure 5.2 to Figure 5.16.

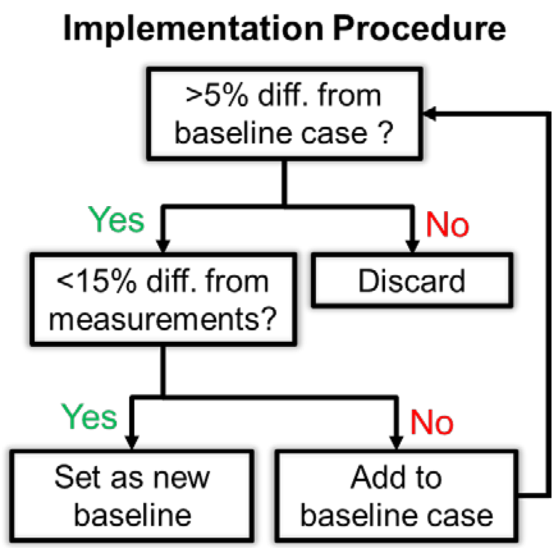

Figure 5.1 TDMP implementation procedure.

Table 5.1 Iteration 1 of TD implementation procedure.

Shell Thick.	% Diff. from Baseline Case		% Diff. from Measurements	
TDP	Line A % Diff	Line B % Diff	Line A % Diff	Line B % Diff
Constant MP	Baseline		**31.1**	**49.9**
T. Cond.	36.8	35.4	57.8	32.7
Density	45.5	12.8	64.0	43.7
S.F. Curve	16.8	53.2	42.8	24.1
Specific Heat	89.8	91.5	94.2	95.8
Viscosity (CSF=0.525)	43.3	97.2	9.0	6.8
Viscosity (CSF=0.725)	43.3	97.2	9.0	6.8
Viscosity (CSF=0.95)	43.8	97.8	8.8	6.8

Table 5.2 Iteration 2 of TD implementation procedure.

Shell Thick.	% Diff. from Baseline Case		% Diff. from Measurements	
TDP	Line A % Diff	Line B % Diff	Line A % Diff	Line B % Diff
T. Cond.	< 5	< 5	< 15	< 15
Density	< 5	< 5	< 15	< 15
S.F. Curve	< 5	< 5	< 15	< 15
Specific Heat	> 5	> 5	> 15	> 15
Viscosity (CSF=0.95)	Baseline		8.8	6.8

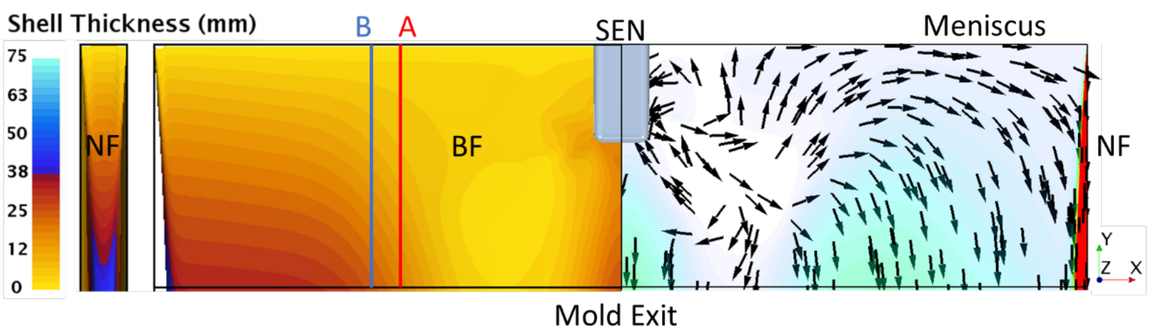

Figure 5.2 Constant MP – shell thickness (left) and flow (right) contours.

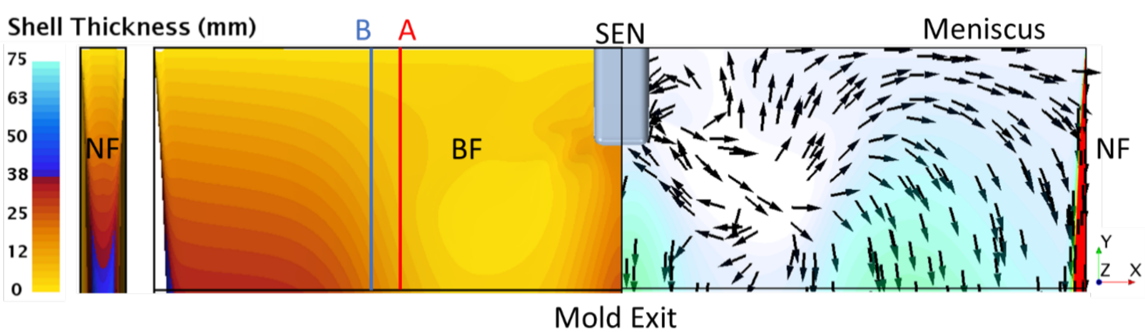

Figure 5.3 TD density - shell thickness (left) and flow (right) contours.

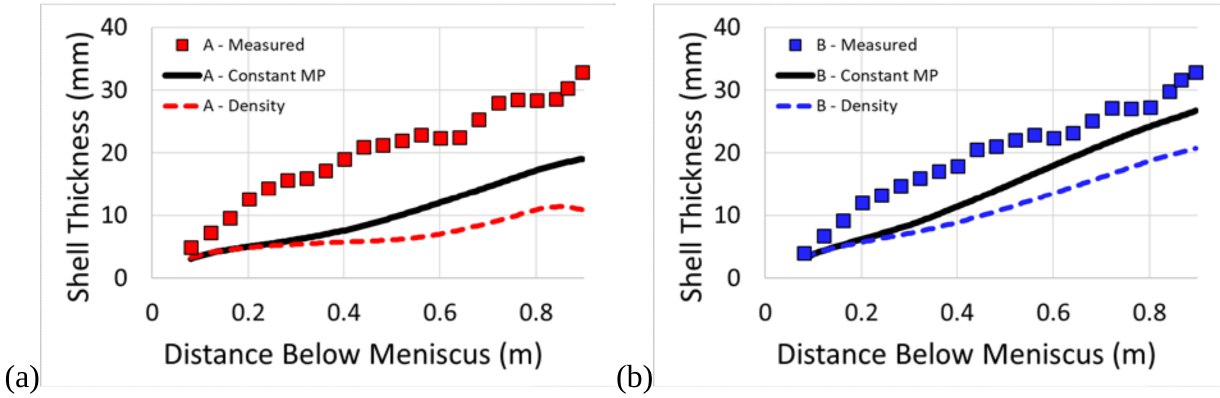

Figure 5.4 TD density - shell thickness comparison plots for: (a) line A, and (b) line B.

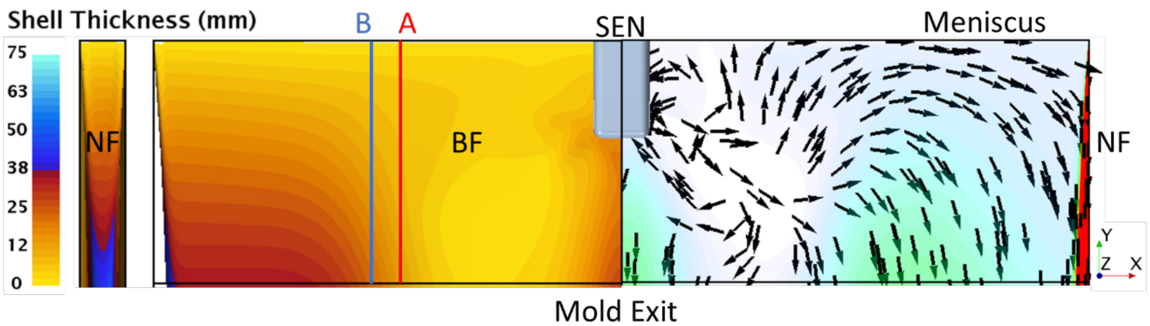

Figure 5.5 TD thermal conductivity – shell thickness (left) and flow (right) contours.

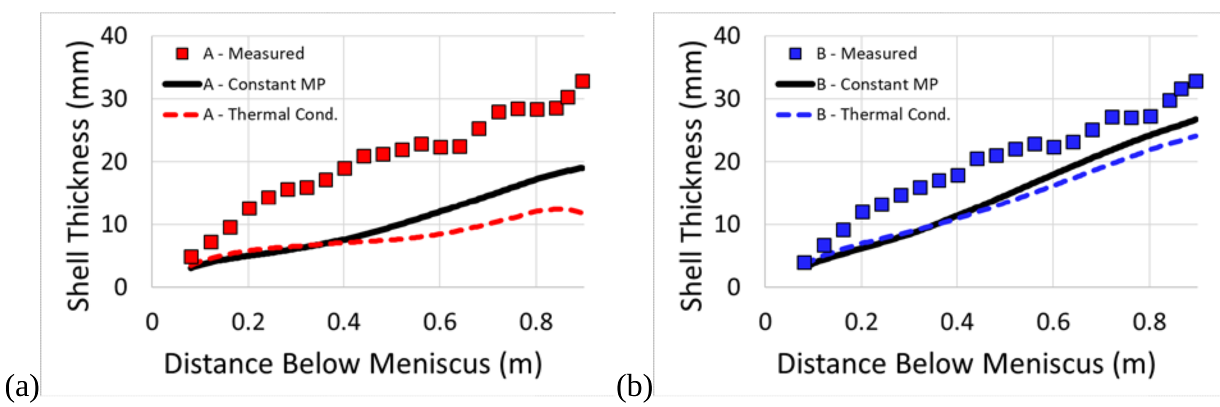

Figure 5.6 TD thermal conductivity - shell thickness comparison plots for: (a) line A, and (b) line B.

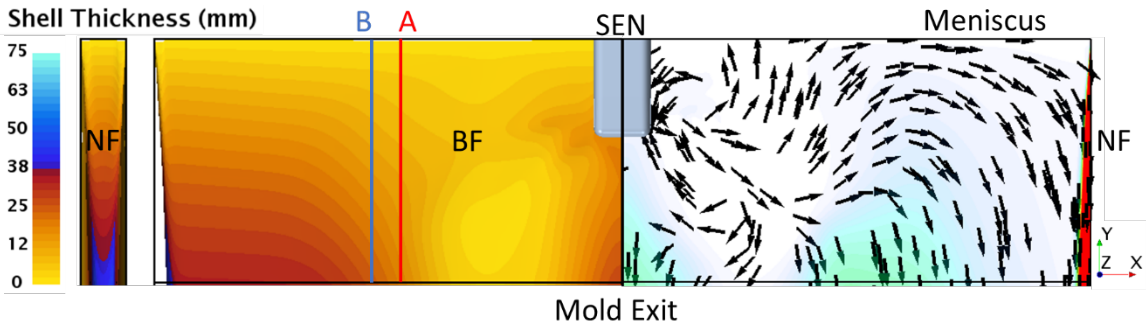

Figure 5.7 TD solid fraction curve – shell thickness (left) and flow (right) contours.

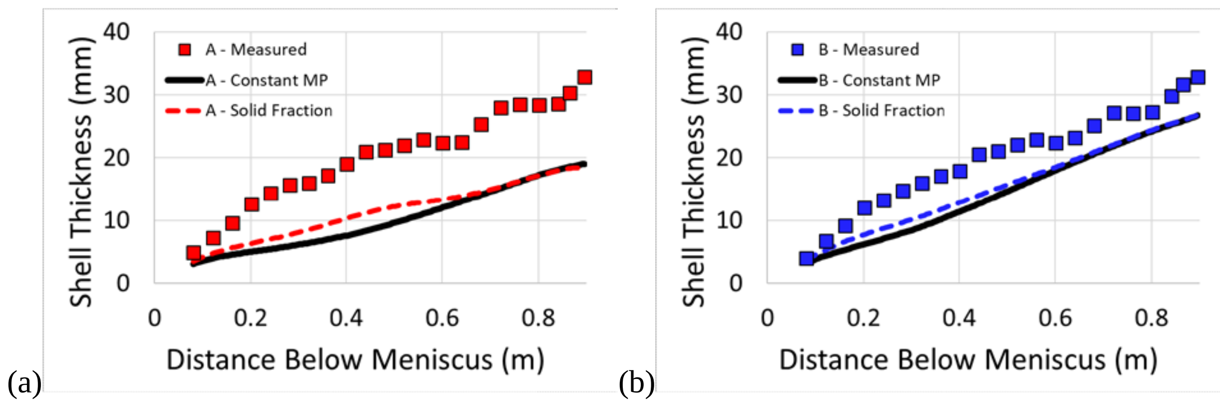

Figure 5.8 TD solid fraction - shell thickness comparison plots for: (a) line A, and (b) line B.

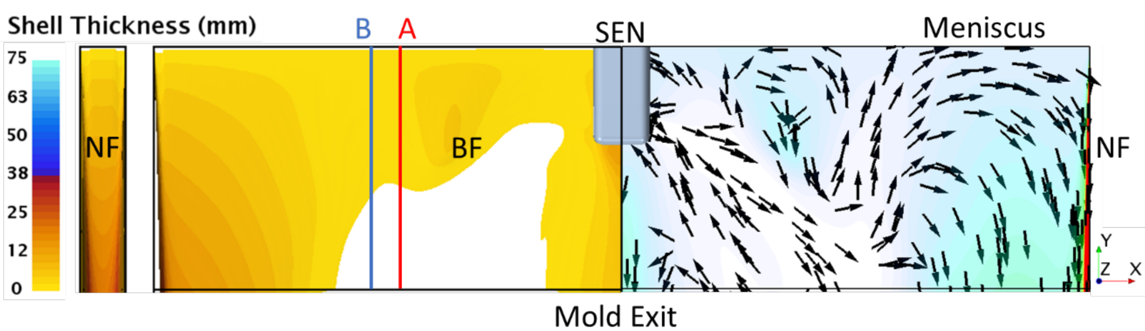

Figure 5.9 TD specific heat - shell thickness (left) and flow (right) contours.

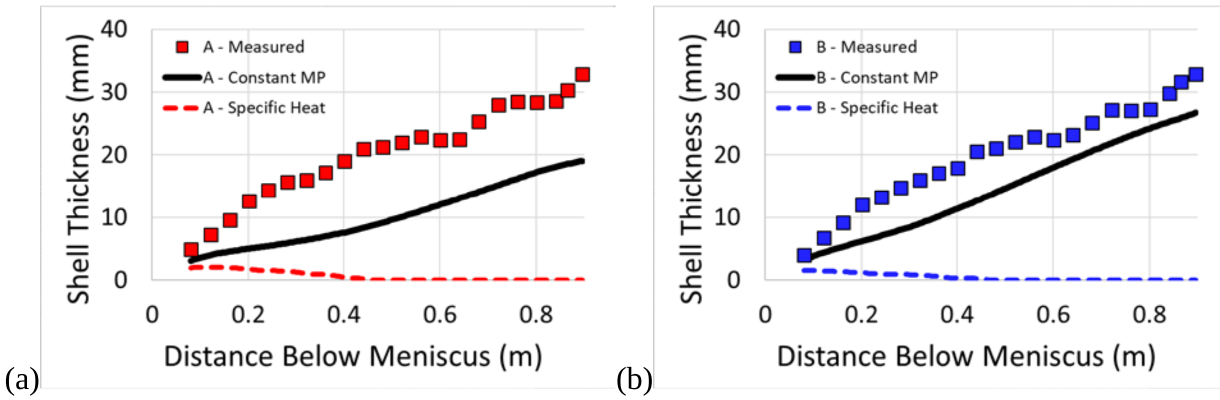

Figure 5.10 TD specific heat - shell thickness comparison plots for: (a) line A, and (b) line B.

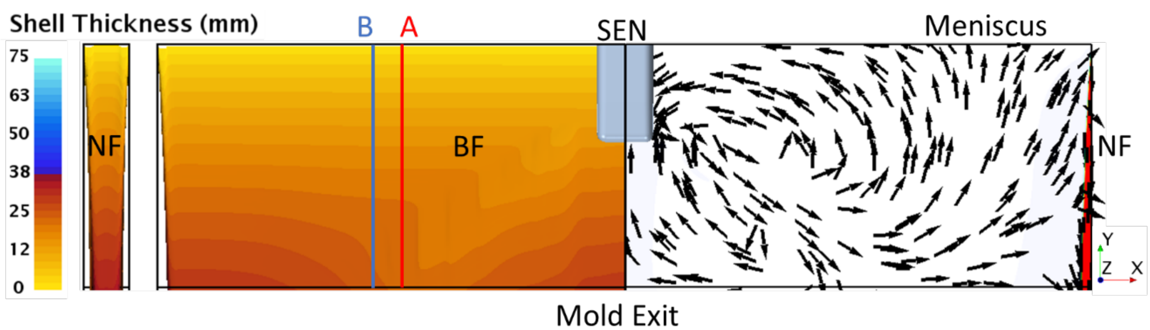

Figure 5.11 TD viscosity at 0.525 CSF - shell thickness (left) and flow (right) contours.

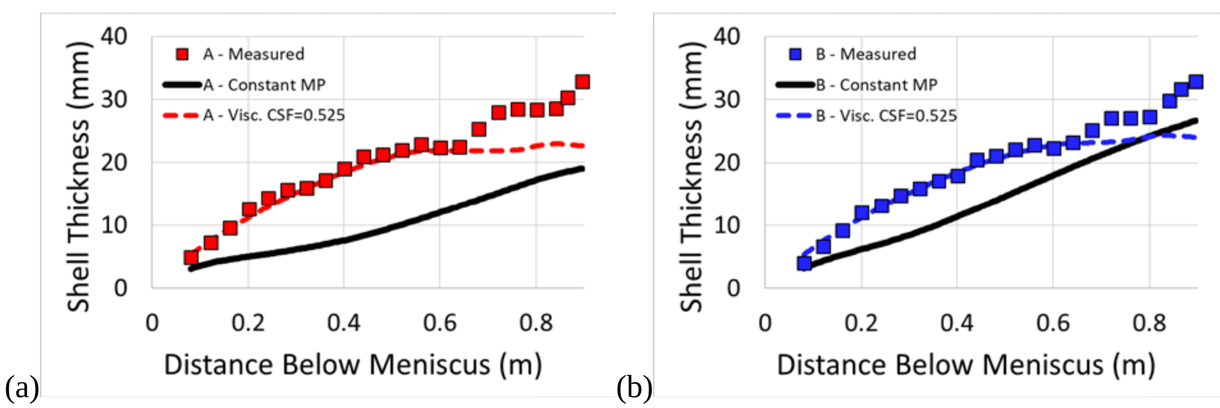

Figure 5.12 TD viscosity at 0.525 CSF - shell thickness comparison plots for: (a) line A, and (b) line B.

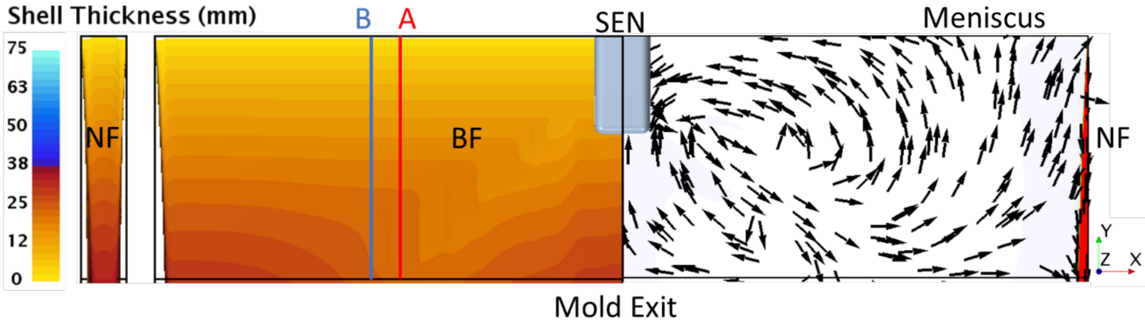

Figure 5.13 TD viscosity at 0.725 CSF - shell thickness (left) and flow (right) contours.

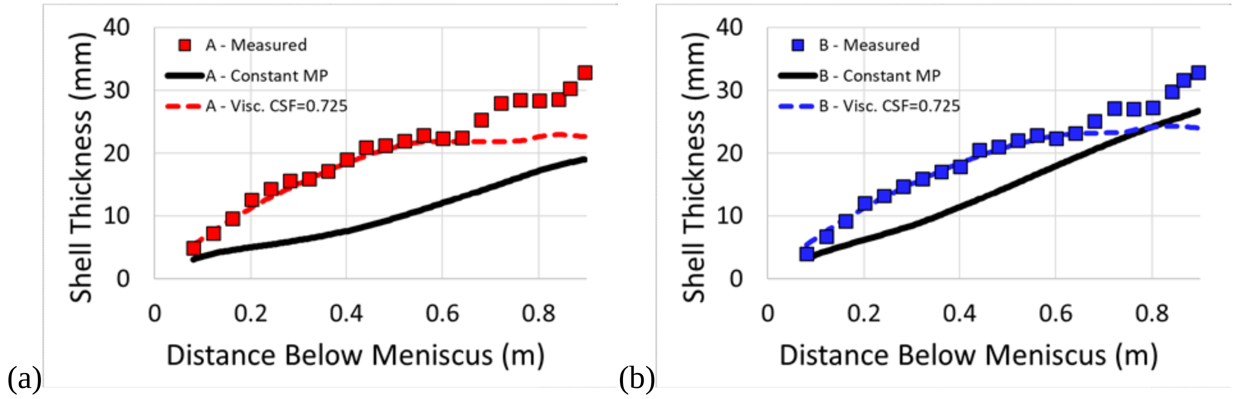

Figure 5.14 TD viscosity at 0.725 CSF - shell thickness comparison plots for: (a) line A, and (b) line B.

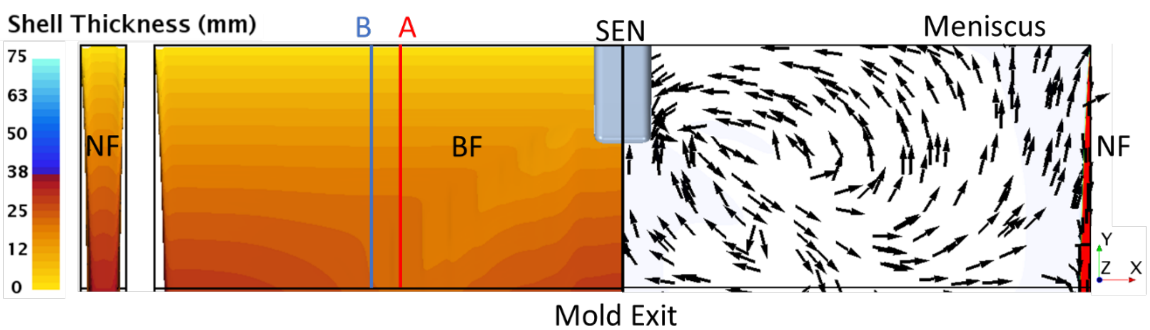

Figure 5.15 TD viscosity at 0.95 CSF - shell thickness (left) and flow (right) contours.

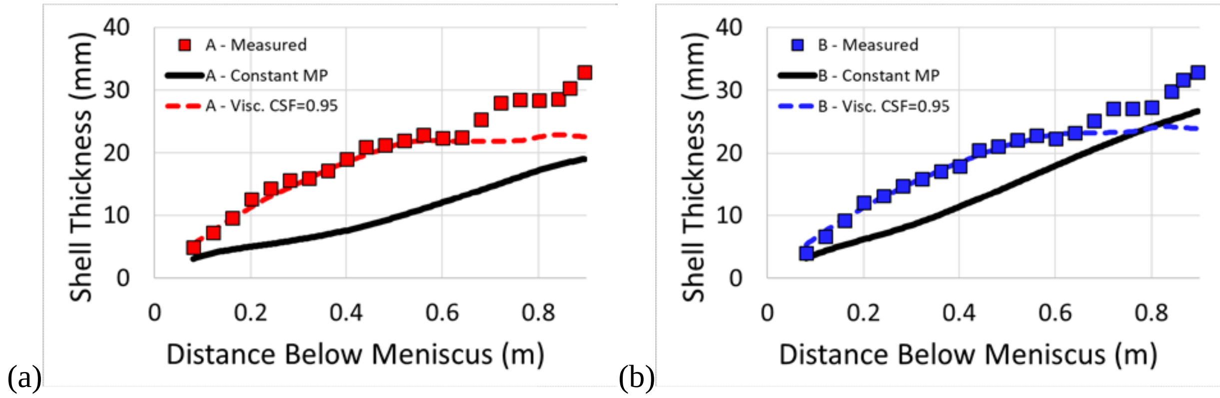

Figure 5.16 TD viscosity at 0.95 CSF - shell thickness comparison plots for: (a) line A, and (b) line B.

Steady-State Validation with TD-Viscosity

The shell thickness was validated with the TD Viscosity case with a CSF of 0.95. The simulation results have an average percentage difference of 7.8% in comparison to the measured segment from the breakout shell as shown in Figure 5.17. Results remain very accurate until about 0.6 m below the meniscus (Line C) where the jet penetrates and distributes the superheat causing slight undergrowth. It is important to note that the casting and cooling conditions at this time were irregular, and also SC spray information was not provided by our IC but interpolated from research. Considering the irregular conditions and SC interpolation the shell growth results may be skewed to not match those from a SS simulation. The shell validation results improved by 7% in comparison to the results with preliminary CMP cases. Not only did the shell growth results improve but the flow field shows better jet penetration and roll patterns.

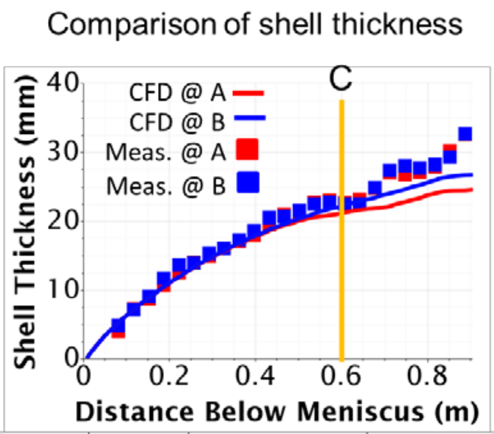

Location	% diff.	Meas. (mm)	CFD (mm)
Line A	8.8	19.9	18.0
Line B	6.8	20.1	18.7

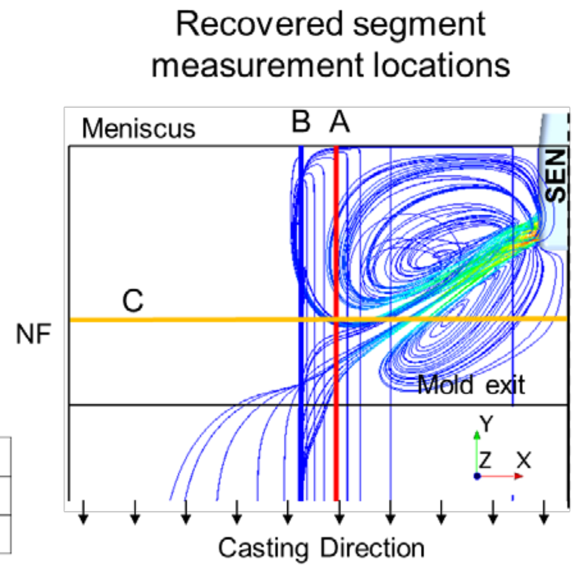

Figure 5.17 SS shell thickness validation with BSM.

Transient Solidification Effects and Validation

The transient solidification project replicated the breakout condition provided to us by IC. The results of the shell thickness and flow field throughout time can be found in Figure 5.18. One can see the shell growth from 40IPM at time 0s to the breakout occurrence at 20IPM at time 103s. The flow field adjust rapidly from 0s to 5s and the jet penetrates at a slightly steeper angle because of the lower casting speed. A comparison of the shell growth throughout time with the BSM at 20IPM can be seen in Figure 5.19. The average difference between the simulated shell at 103s with the BSM was 10%. The percentage difference is slightly off in comparison to the 20IPM SS case at 8% showing that in this particular case the SS simulation is sufficient in validating shell growth. However, the transient case more accurately models the shell growth and flow throughout time because of its variable casting BCs. A comparison of the two validations is displayed in Table 5.3

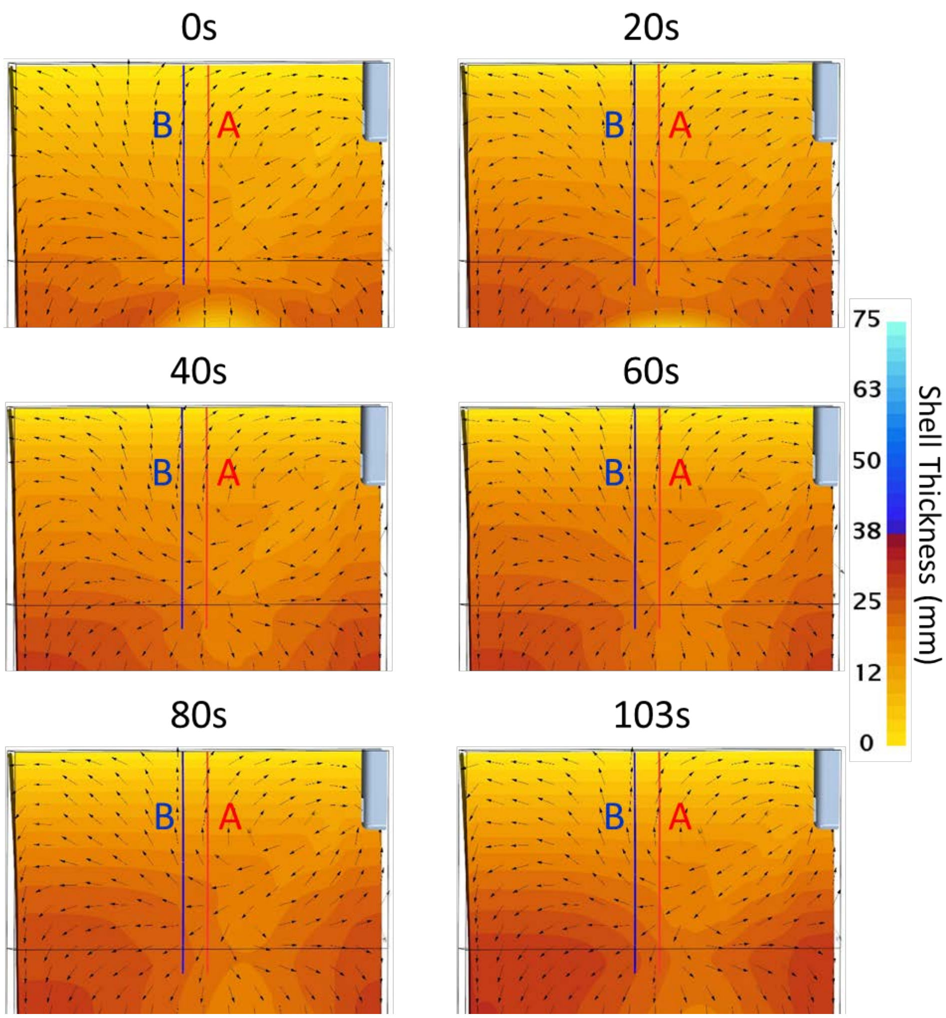

Figure 5.18 Shell thickness contour evolution.

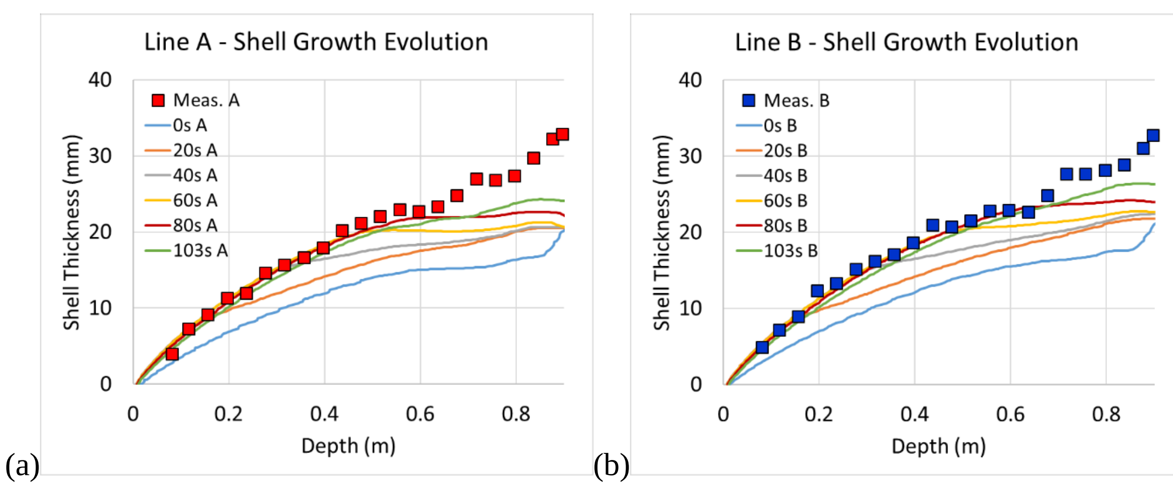

Figure 5.19 Shell growth evolution through time: (a) line A, and (b) line B.

Table 5.3 SS and transient solidification validation comparison.

Location	Model	Meas. (mm)	CFD (mm)	% diff.
Line A	Steady-state model	19.9	18.0	8.8
	Transient model		17.6	10.9
Line B	Steady-state model	20.1	18.7	6.8
	Transient model		18.4	9.0

5.1.2 Solidification Carbon Percentage Parametric Investigation

Four different alloy compositions were investigated with varying carbon percentages in order to analyze the effect on flow and shell growth. A plot showing the comparison of both the flow field and shell thickness contour can be seen in Figure 5.20. The jet penetration increases as the carbon percentage decreases, this is likely due to the decreasing viscosity trend mentioned in the BC section. Less resistance is added to the flow and therefore there is deeper penetration. The shell thickens as carbon percentage decreases and this is likely due to the decreasing MZ range trend explained in the BC section. Smaller MZ ranges associated with lower carbon percentages require less energy to convert molten steel to solidified steel, additionally deeper penetrating jets associated with lower carbon percentages allows for a better distribution of heat. A shell thickness comparison plot can be seen in Figure 5.21 where the shell thickness trend becomes clearer.

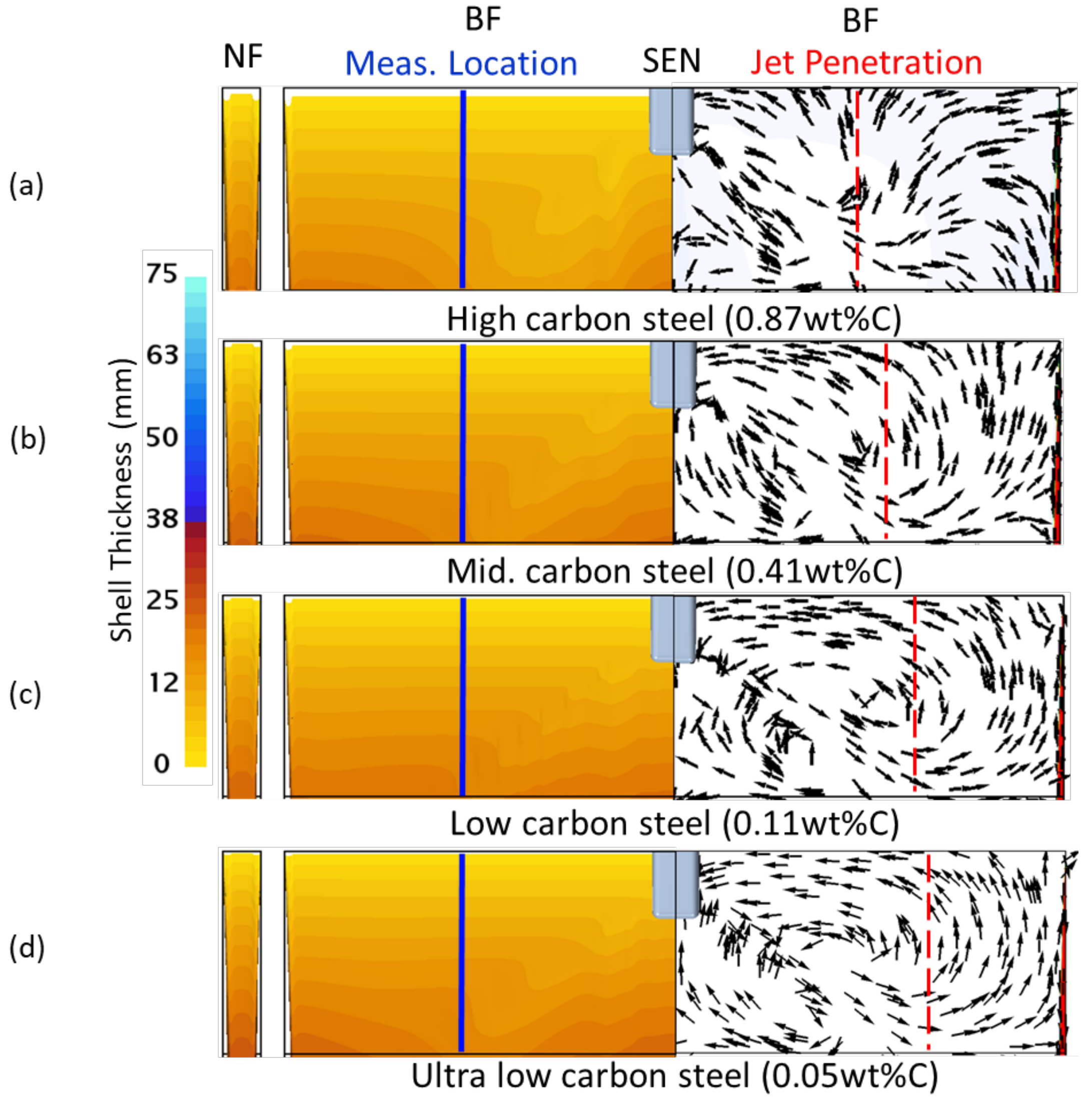

Figure 5.20 Shell thickness (left) and flow (right) contours of carbon percentage study: (a) HCS, (b) MCS, (c) LCS, and (d) ULCS.

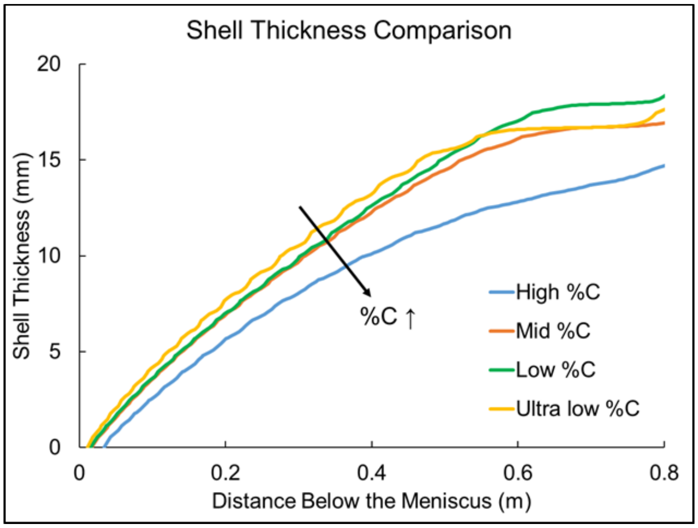

Figure 5.21 Shell thickness comparison for carbon percentage analysis.

5.2 Thermal-Mechanical Stress

This section presents the results from all the thermal-mechanical stress cases. As mentioned in section 2.2, the validation for stress inside the shell during the casting process is nearly impossible because of the inherently high temperatures and constantly moving components. Therefore, a 1D analytical solution and CON2D simulations were used for validating stress-strain constitutive relations [20], [21].After validating the PP stress relation, more assurance was needed for the 3D model so the validated relations were applied to a quarter section of the shell and compared to Koric and Thomas's work for a pseudo-validation [29]. The PP relation was then applied to the larger half portion of the 3D shell to analyze the effects of mesh on overall deformation. In order to add to the complexity and accuracy of the model the more realistic VP stress-strain relation was validated. This stress relation and mechanical TDMP were applied to the 3D quarter shell at different cast speeds and using different compositions to analyze the effect on stress and displacement.

5.2.1 Stress Relation Validation

The problem proposed by Weiner and Boley considers a 1D idealization of the early stages of solidification casting in a mold, as shown in Figure 5.22. The problem is simple, the molten steel is introduced to the cold mold wall set at a low temperature below the solidus temperature of the steel. As time passes the cold mold wall will cool the molten core and the shell will thicken. The cooling process creates a temperature gradient within the solidified portion which creates stress within the shell. They assume that this small slice can represent a uniform section of the shell by applying symmetry BCs. Therefore, the thickness of the shell will remain constant along the width direction. The 1D assumption takes advantage of the long width of the shell along the mold wall and utilizes generalized plane stress.

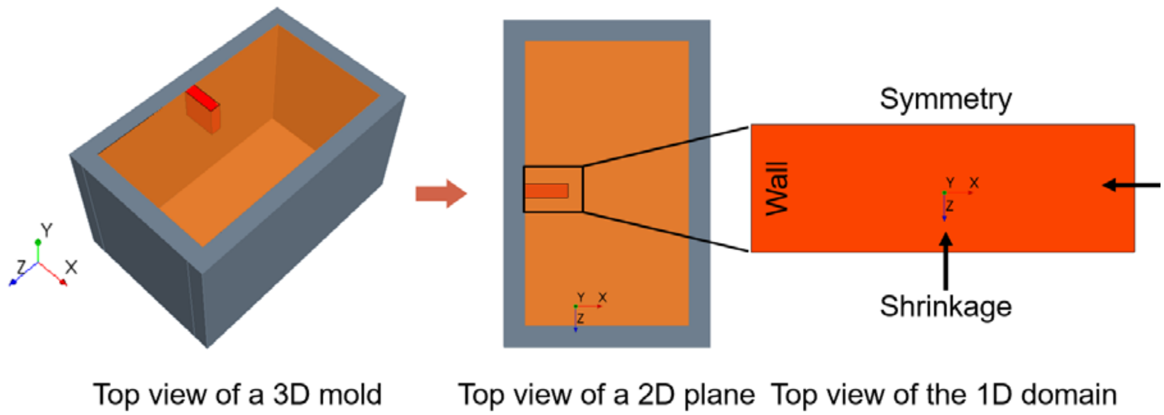

Figure 5.22 Location and simplification of the solidifying slice.

The first constitutive relation used in this work was the PP model. Weiner and Boley treat yield stress as a linear function of temperature starting from 20MPa at 1000°C to 0MPa at the solidus temperature of 1494.4°C. They also assume a small MZ region to avoid the difficulties of modeling creep strain. The normal displacement of the bottom surface is treated as zero. Tangential stress is assumed to be zero along all surfaces because of the assumption of generalized plane stress. Lastly, the top surface of the domain is fixed to remain vertical to avoid bending along the x-y plane. The BC for the solidification and stress simulation are shown in Figure 5.23. All the MP constants used in this PP solidification and stress validation are listed in Table 5.4.

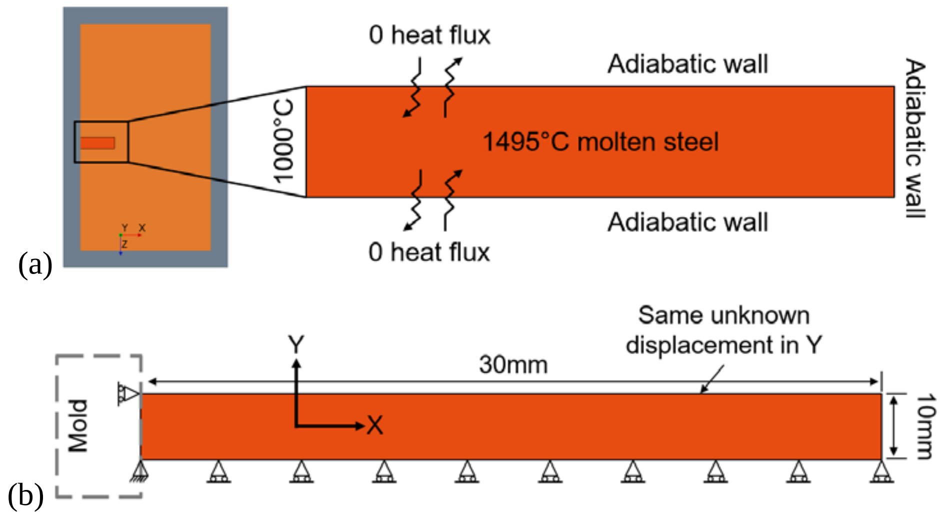

Figure 5.23 BCs: (a) solidification simulation, and (b) stress simulation.

Table 5.4 MP constants used in PP validation.

Parameter	Value
Conductivity (W/m-K)	33
Specific heat (kJ/kg-K)	661
Elastic modulus in solid (GPa)	40
Elastic modulus in liquid (GPa)	14
Thermal linear expansion coefficient (1/K)	0.00002
Density (kg/m^3)	7500
Poisson's ratio	0.3
Solidus temperature (°C)	1494.4
Initial temperature (°C)	1495
Latent heat (J/kg-K)	272000
Viscosity (Pa-s)	6.667×10^{-9}

Figure 5.27 shows the shell thickness growth and temperature distribution in comparison with Weiner and Boley's analytical solution and Thomas's CON2D simulation for two different times. One can see the shell growth from the mold wall on the left to the shell front at the solidus temperature when the curves flatten. The results align well with both the analytical solution and CON2D simulations with a percentage difference of less than 1%. The zz-stress results for these two times are compared in Figure 5.25. One can see the mold wall, shell front locations, and plastic-elastic-plastic relation which is iconic of a solidifying body. Most of the results remain within a 10% margin of error with a few outliers in the transition from the compression to the tension region and close to the shell front.

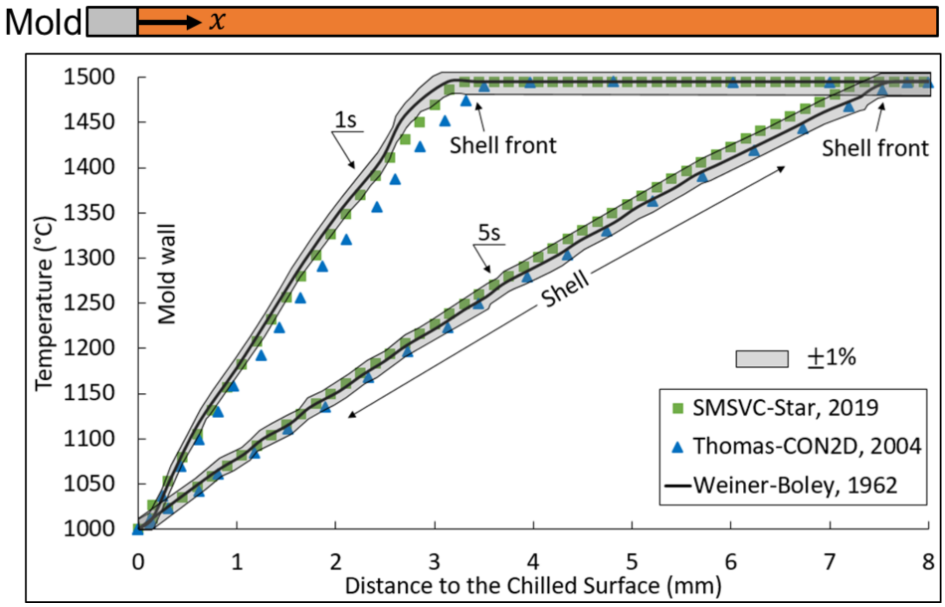

Figure 5.24 Temperature distribution comparison for PP stress relation case.

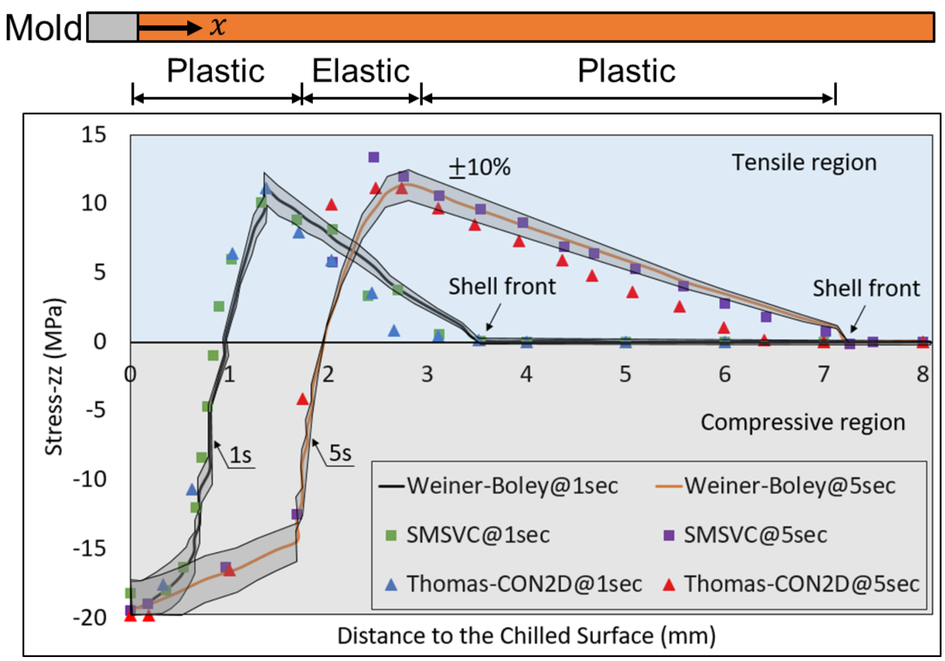

Figure 5.25 Stress distribution comparison for PP stress relation case.

Koric and Thomas expand on this relation including a MZ and incorporation of time dependent creep and flow strains [21]. They also incorporate TDMP for both solidification and stress simulation. The MZ range is about 90°C with T_{sol}=1411.79°C and T_{liq}=1500.72°C. The addition of the flow and creep strains could dramatically change the constitutive stress-strain relationship as seen in Figure 5.26. The PP relation will often not capture a large amount of the stress which the VP case can capture because of the lack of these two additional strains. The shell growth for this proposed case through time is visually represented in Figure 5.27. A comparison of the temperature distribution results with CON2D solutions are in good agreement and have a less than 1% difference, as seen in Figure 5.28.

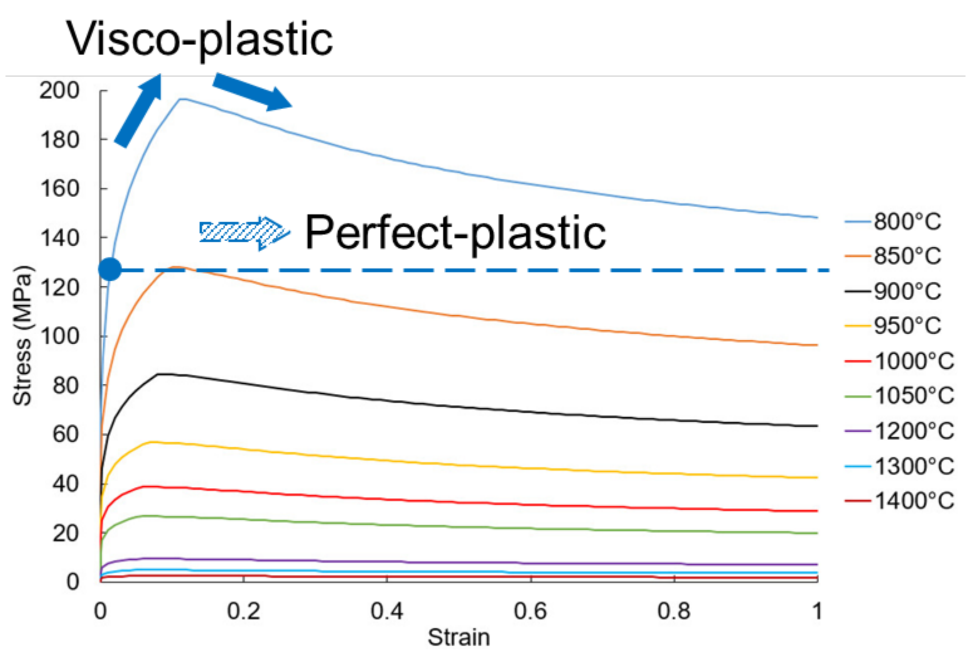

Figure 5.26 VP stress-strain relation presented by Koric and Thomas compared to PP relation.

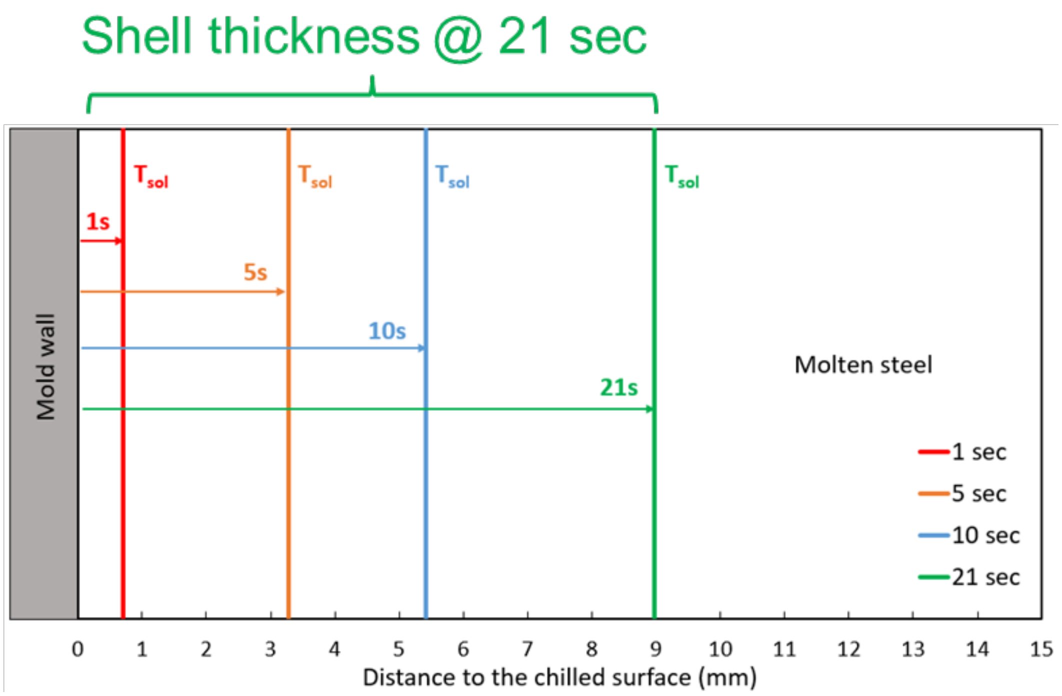

Figure 5.27 Simulated temperature distribution in the solidifying body for VP relation.

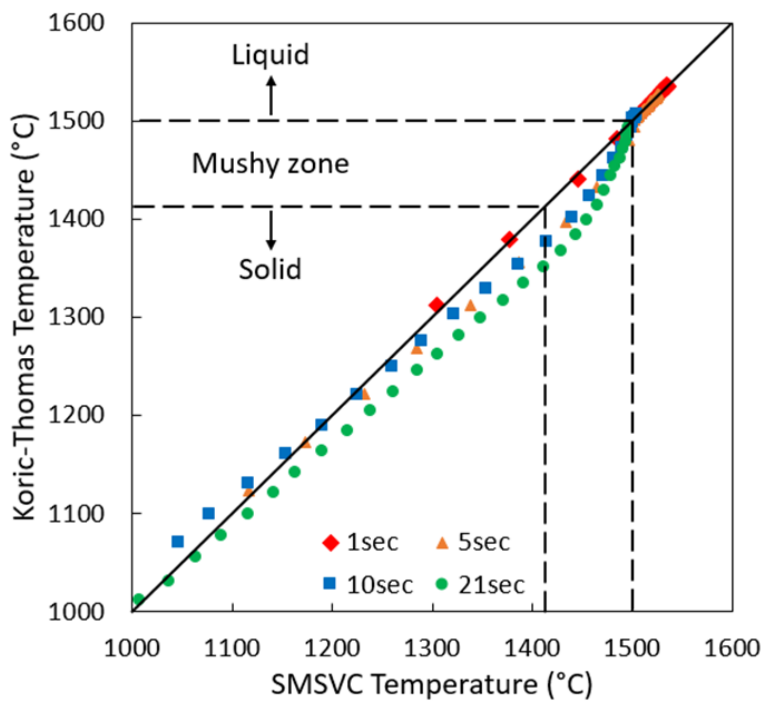

Figure 5.28 Temperature distribution in the solidifying body at different time.

Initially the PP relation was used to try and capture the VP relation in order to validate the MZ case presented by Koric and Thomas. The PP relation could imitate most of the VP relation but the simplistic nature was not completely sufficient and results showed an average difference of 27%, as shown in Figure 5.29. The results were improved by using UDFs in Star-CCM+ to replicate the distinctive plastic behavior the VP relation exhibits. The average difference after implementing these UDFs was 12% which shows good agreement with Koric and Thomas's simulations with the improved creep and flow strains.

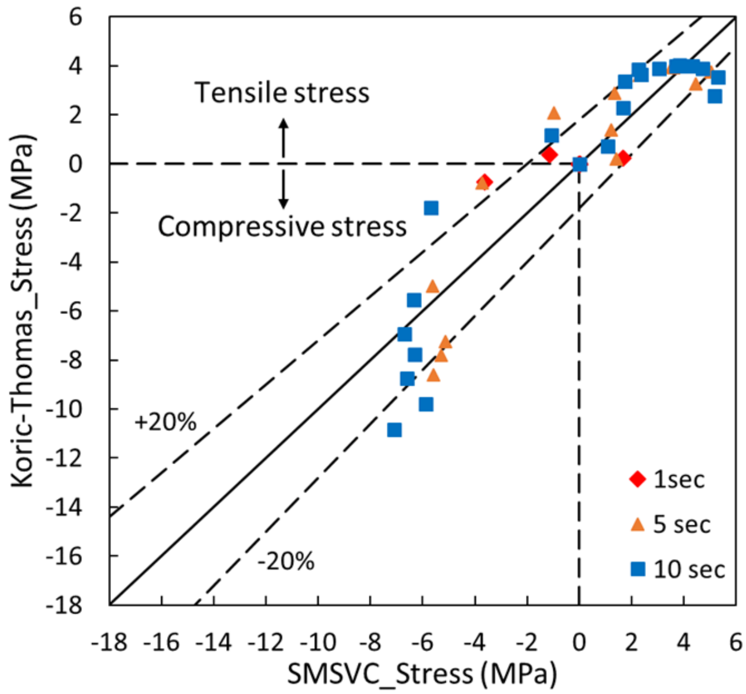

Figure 5.29 Stress distribution in the solidifying body at different time for PP relation.

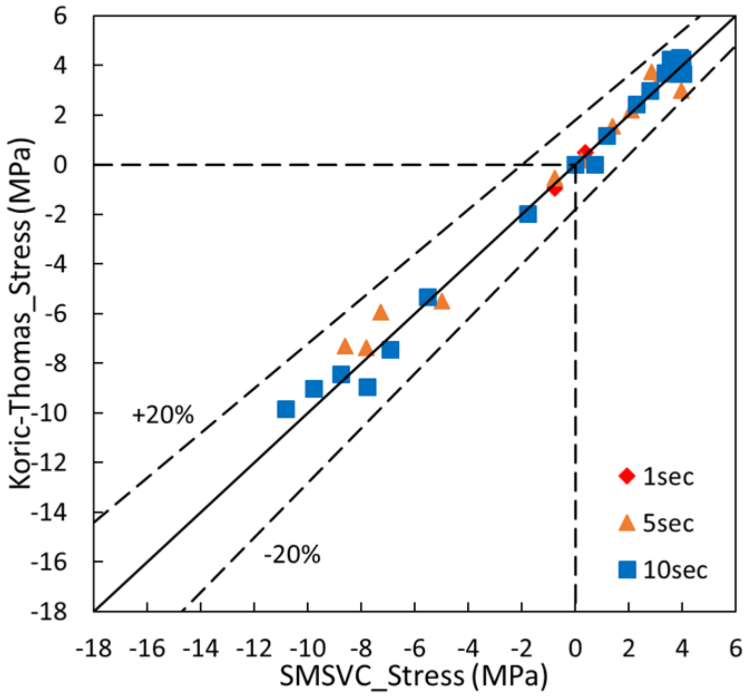

Figure 5.30 Stress distribution in the solidifying body at different time for VP relation.

5.2.2 3D Shell Simulations

Half Shell Pseudo-Validation

The 3D quarter shell pseudo-validation with Koric and Thomas work is shown in Figure 5.31 [29]. Note that the caster geometries, casting conditions, and steel compositions are all different and this case was made to compare trends. A similar temperature distribution is shown with intense cooling in the corner and a transition to high temperatures towards the shell front. Y-stress distribution shows a similar trend and distribution as well with compression along the BF and tension near the corner and NF. Only TD yield stress was used in this simulation. Standard 1020 steel MP at room temperature were utilized for simulating the stress, which were similar to the solidification MP [35].

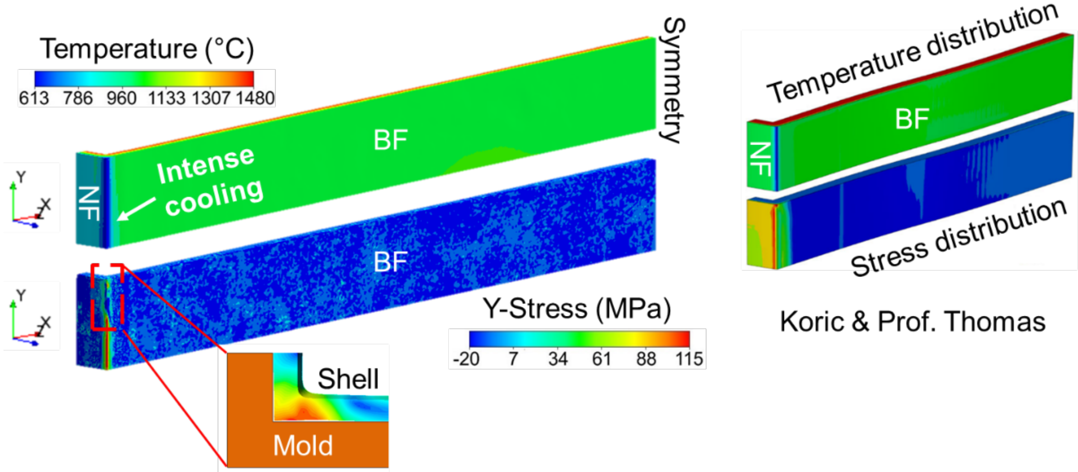

Figure 5.31 3D quarter shell pseudo-validation comparison.

3D Half Shell Simulations

The half shell simulations utilize the PP stress relation and CMP. One can see the deformation of the half shell utilizing a 10mm mesh base size and 5mm mesh base size in Figure 5.32 and Figure 5.33, respectively. The 10mm base size mesh increases max deformation by more than 20mm in comparison to the 5mm base size mesh. The excessive inward deflection of the shell near the meniscus in the 10mm base size simulation is likely due to its inability to correctly model bending because of the limited amount of cells in the thinning part of the shell. Therefore, it is recommended to use a finer mesh size towards the meniscus so the amount of bending is modeled more accurately. A corner mesh refinement of 2mm was placed in the corners for both simulations that is why they exhibit similar deformation along the corners where the shell experiences shrinkage due to increased cooling. Overall, the results show the stereotypical phenomena of a shell within the mold such as air gap formation, corner shrinkage, and inward deflection of the thinning portion of the shell because of low ferrostatic pressure and bending stresses.

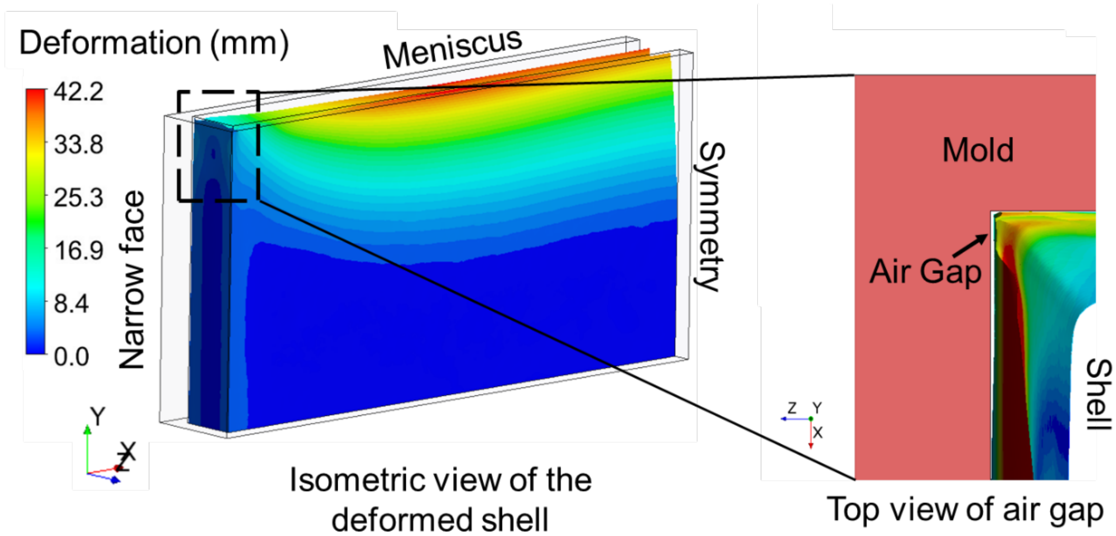

Figure 5.32 10mm mesh base size - half shell deformation.

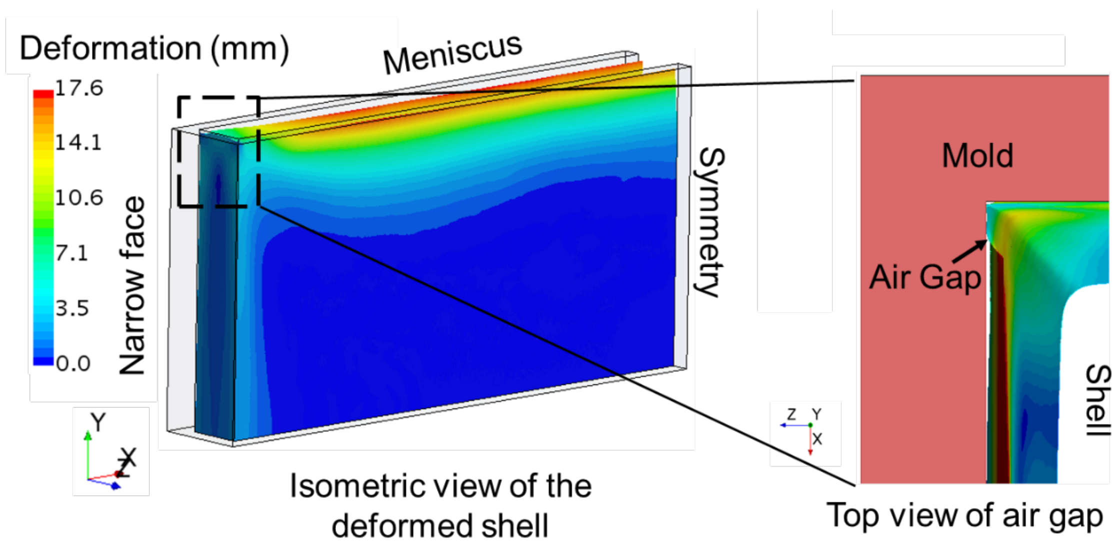

Figure 5.33 5mm mesh base size - half shell deformation.

Breakout Steel 3D Quarter Shell Simulations with TDMP

The following cases incorporate TDMP for young's modulus, thermal expansion coefficient, density, Poisson's ratio, and plastic strain. Three quarter shell cases are used to show the deformation comparison of stress relation and casting speed as displayed in Figure 5.34. The PP deformation shows a similar displacement trend in comparison to the VP case along the BF but predicts 3x larger displacement at the NF. The PP relation likely over predicts deformation because of its simplification of stress being constant once the yield point is surpassed. Comparing the 40IPM VP case with the 20IPM VP case one can see that displacement increases along the width of the BF and by roughly 2mm at the NF. It would be recommended to use a larger mold taper at lower casting speed and this is supported by BG Thomas mold taper literature for a thin slab caster [24].

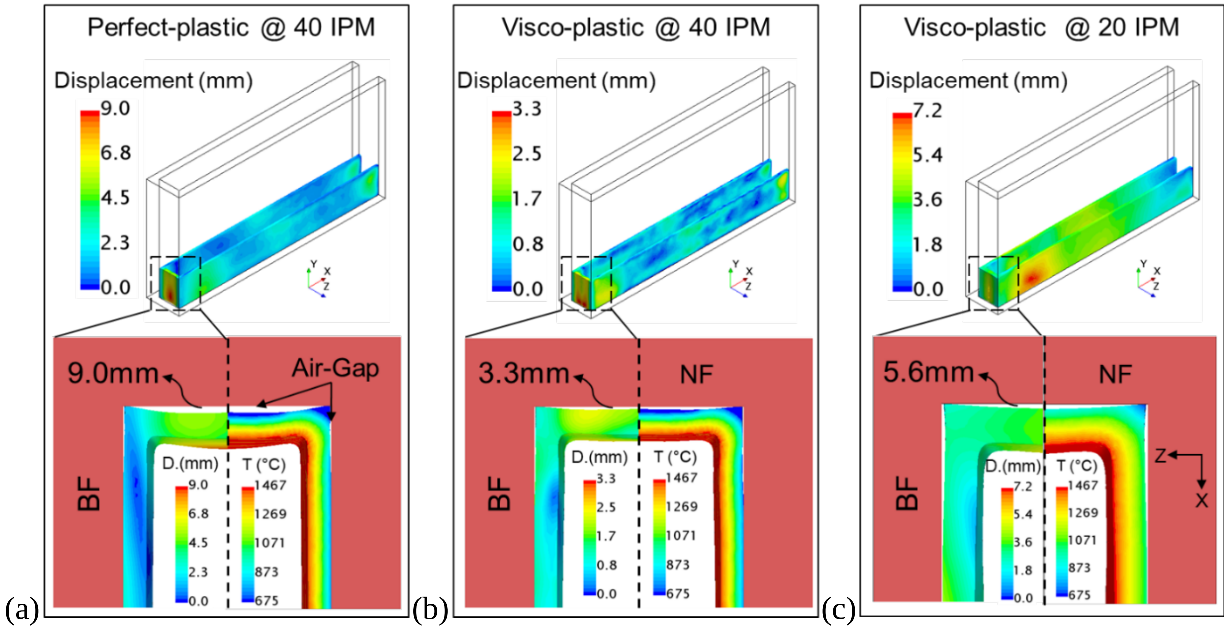

Figure 5.34 Displacement and temperature distribution comparison of stress relations and casting speed: (a) PP at 40ipm, (b) VP at 40ipm, (c) VP at 20IPM.

An analysis of the stress accumulation in these three cases is shown in Figure 5.35. Stress is higher in the VP case in comparison to the PP case because the PP stress relation does not account for the more complex creep and flow strain that would increase the stress rather than treat it as constant past the yield point. The VP case at 40ipm has higher stress than the 20ipm VP case because of the lower temperatures and higher temperature gradients found in the 40ipm case. The stress is highest at the NF and decreases as the probe approaches the shell front which is consistent with the thermal-mechanical behaviors of a solidifying body. Higher temperatures are closer to the shell front and are associated with lower stress yield points, as one gets closer to the NF the temperature decreases and the solidified body allows for more stress accumulation.

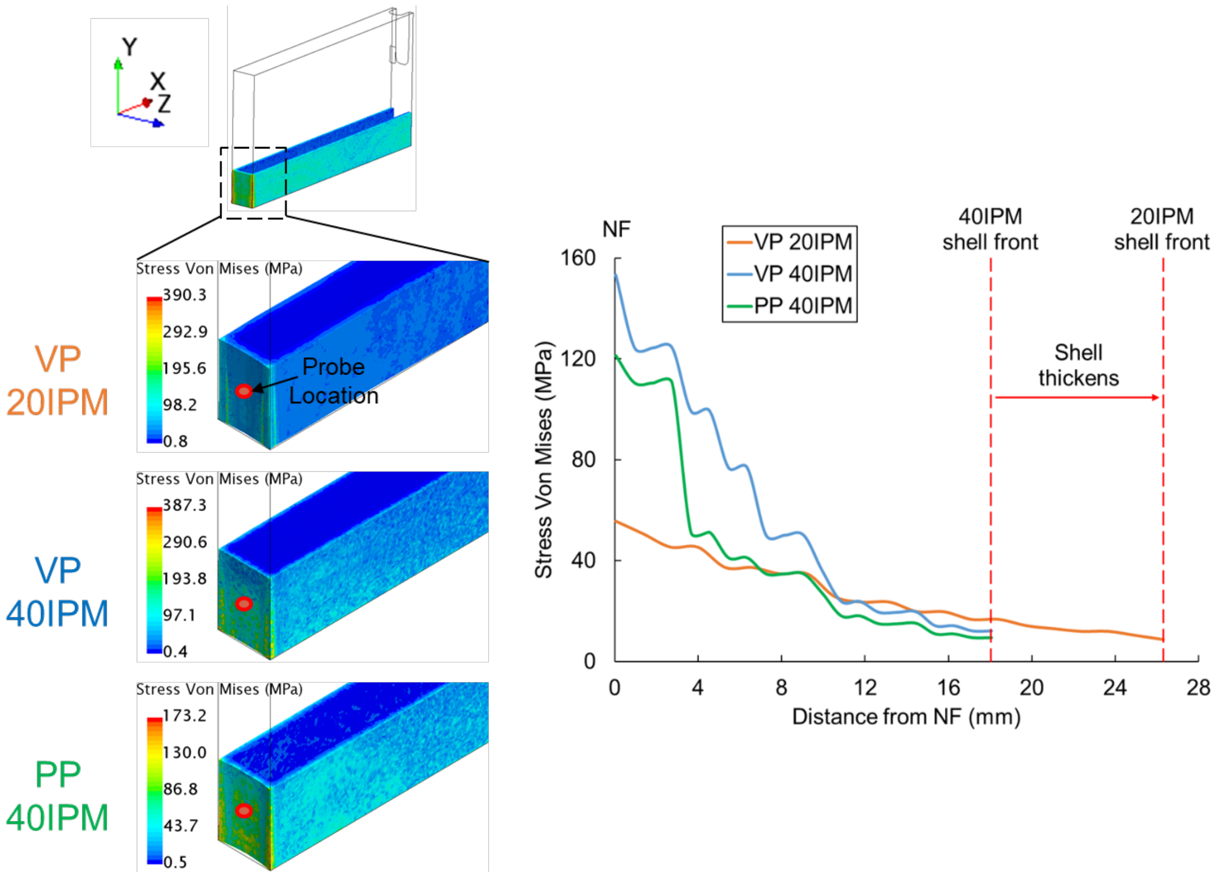

Figure 5.35 Von Mises stress distribution comparison of stress relation and casting speed at the center of the NF.

Carbon Percentage 3D Quarter Shell Simulations with TDMP

Displacement distributions for the four different alloys in our carbon percentage analysis are shown in Figure 5.36. The deformation doesn't follow any grand trends with carbon percentage as it did with solidification but is shown to be more complex in nature because of the many intricate thermal-mechanical factors. Thermal-mechanical MP, temperature gradient, and BCs all play a role in the deformation of the shell. The NF displacement ranges from 2 to 5mm which is consistent with BG Thomas's work for a thin slab caster [24]. That same work predicts that ULCS will need an increased NF mold taper and our results show that to be true. The HCS and MCS have similar BF and NF displacement trends likely due to their stiff nature. The LCS and ULCS have similar displacement trends with less displacement along the BF and more at the NF. The ferrostatic pressure likely plays a greater role in lower carbon steels because of their ductility and this will push the shell closer to the BF which will intuitively decrease the displacement inwards.

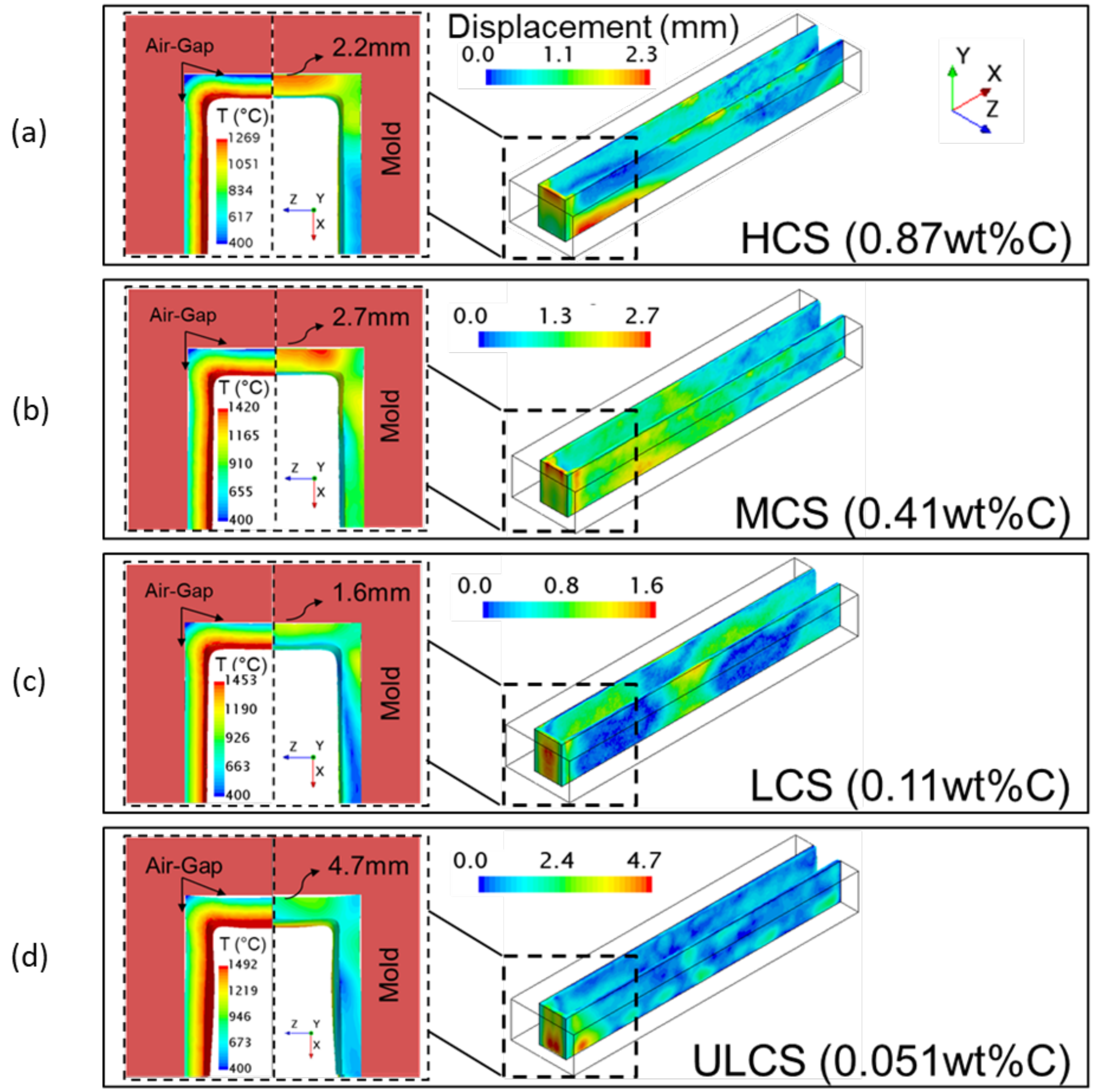

Figure 5.36 Displacement and temperature distribution comparison for carbon percentage study: (a) HCS, (b) MCS, (c) LCS, and (d) ULCS.

5.3 Model Applications and Future Work

5.3.1 Flow and Solidification Model - Now & Future

The current F&S model uses an adaptation of the CKMZ model by using TD-total viscosity to govern most of the flow. The results were validated well with the BSM with an average percentage difference of 8%. However, the flow within the simulation was not completely ideal and the jet would often split before reaching the NF. The CKMZ model is likely adding excessive dampening to the fluid which is already being adjusted by the TD-viscosity. A future F&S model would discard the CKMZ model and rely on the total viscosity completely. It was not done in this model because the CKMZ increased the convergence and allowed for a pull velocity to be easily applied to the solidified shell within Star-CCM+.

Within Star-CCM+ a user-defined (UD) MZ can be implemented within the solidification model. A future model would use this UDMZ to stop the flow and apply a pull velocity rather than the current method with the adapted CKMZ. This model would require a parametric study to determine the correct amount of MZ needed to simulate the solidification accurately. The correct amount of MZ would be fine-tuned to match the BSM and adjusted overtime to match other breakout shells until a correlation is made. However, obtaining BSM is a difficult task because they are often proprietary. At the very least the model could be fine-tuned for a particular caster and could be used to get flow and shell growth estimations.

5.3.2 Thermal-Mechanical Stress Model - Now & Future

The future of the stress model would include further expansion of the shell from the current quarter shell simulations. The model was facing divergence issues when trying to implement the VP stress relation and TDMP into the half shell. The divergence was likely due to the excessive amount of deformation that was occurring because of bending, and as noted in section 5.2.1, the model assumes small strain. More time is needed to investigate a numerical and mesh method that would allow for a converged solution. If the shell cannot be expanded towards the very thin portion of the shell close to the meniscus, a few symmetry BC could be exchanged for an extended portion of the shell to examine the impact each symmetry condition has on stress and deformation. There are many routes in which the current model can go from here, but some of the many options include: a hook formation study, crack detection, or a more expansive corner shell shrinkage study. All these models would be application driven and could be used to provide information to ICs such as cooling suggestions or potential mold taper designs. Ideally the solidification and stress models should be integrated more closely in order to further the accuracy of each, the next section proposes a methodology to connect the two more closely.

Corner Offset Solidification and Stress Iterative Procedure

After simulating the thermal-mechanical behaviors for all the different cases which include casting speed and alloy composition changes it was clear that air gap formation would vary between each case. The current assumption used within all of the solidification models is a reduced corner HFP of 31mm based on literature as described in section 4.2.2. This assumption of 31mm could over predict or under predict the actual cooling that occurs in the corners. Incorrect cooling can result in unrealistic shell thickness, temperature gradient, and consequently the stress and deformation. Therefore, a model that connects the two simulations strongly would be optimal for obtaining accurate results.

This iteration procedure would first start with the 31mm corner offset assumption for the reduced cooling in the solidification simulation. After obtaining the shell and simulating the displacement one could obtain the air gap length along both the BF and NF for each corner. A threshold could be used for the air gap to determine if the reduction in the HFP is needed. For example, if the air gap is greater than 1mm from the mold wall it is assumed that the reduction in the HFP is needed. Once the length of the air gap on both the BF and NF is determined, the SP HFP corner offset lengths can be updated within the solidification model. The same procedure can be done again until the air gap lengths experience little change in comparison to the previous iteration. An example of this iterative procedure can be found in Figure 5.37 where CO stands for corner offset. In this example the iteration procedure stops at 3 iteration because the corner offset converged to 45mm x 85 mm for both iteration 2 and iteration 3.

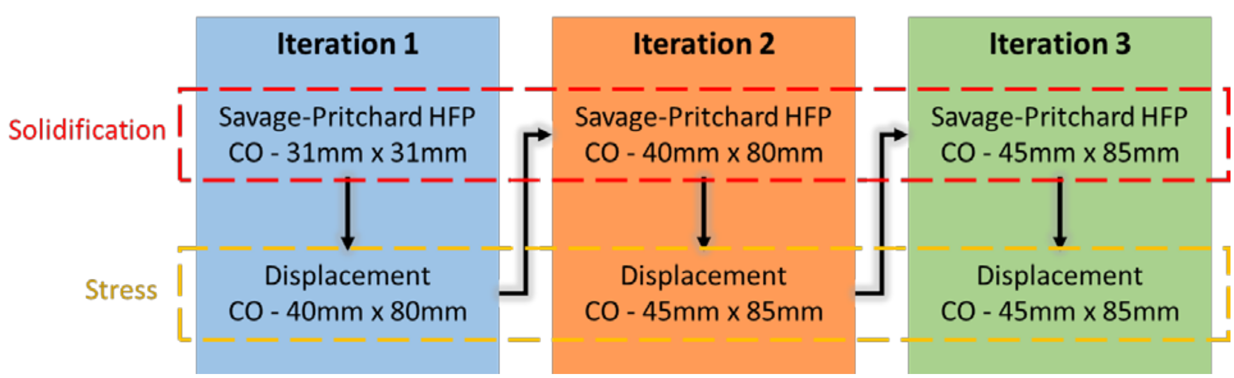

Figure 5.37 Corner offset solidification and stress iteration example.

5.3.3 Integrated Casting Model

As mentioned in section 3.1 the current work is a part of a larger project for a comprehensive casting model. In order to have this fully comprehensive model we must be able to connect the many intricately connected portions from the microscale to the macroscale. The comprehensive model has completed microscale simulation for dendrite arm spacing which provides flow characteristics in the solidification model. Extensive research has been completed on spray cooling and stress in the SC region. Data from the SC model could be fed upstream to the PC model and vice versa to further the accuracy of both the solidification and stress. For example, the temperature and flow data produced in the PC region at the mold exit could be passed to the SC region in order to predict accurate shell growth downstream. The SC spray modeling can be used to create more realistic BC in the PC solidification model in order to predict shell growth shortly below the mold more accurately which could further improve the validation results. A diagram showing the integration methodology can be seen in Figure 5.38.

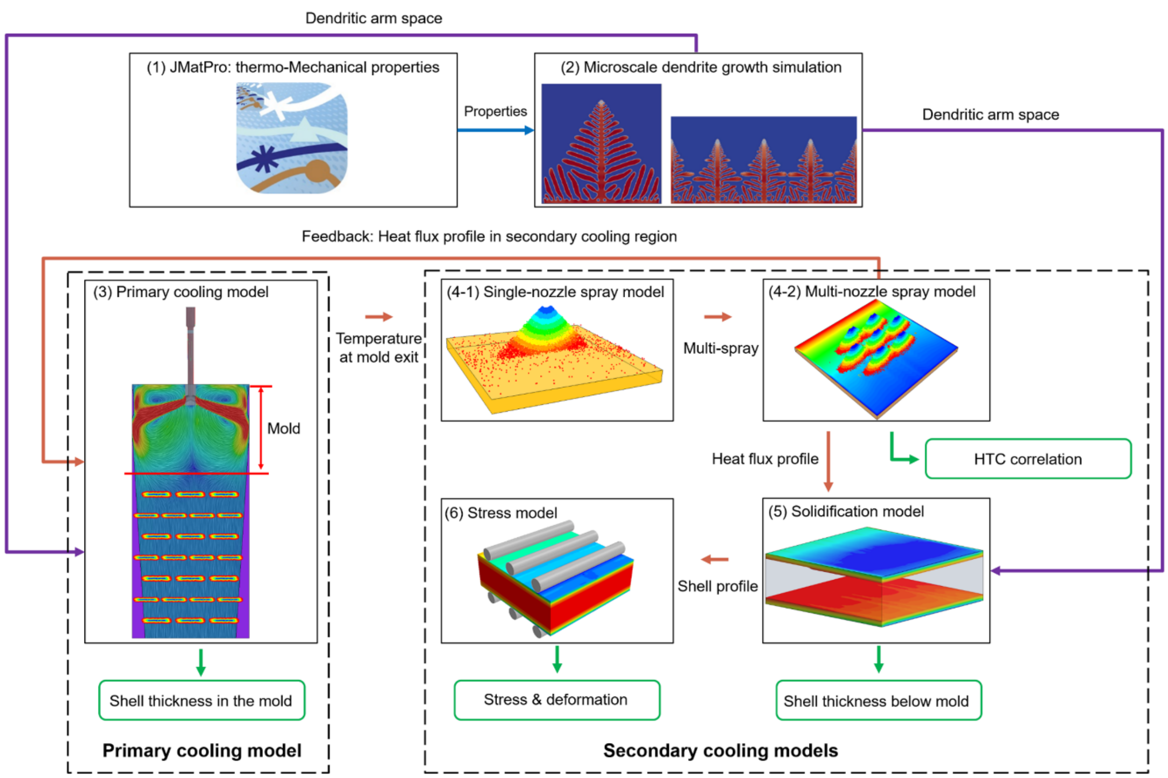

Figure 5.38 Comprehensive model integration methodology.

6. CONCLUSION

A comprehensive model for PC is a necessity when determining complex phenomena such as solidification, and thermal-mechanical stress. The incorporation of TD-Viscosity increased breakout shell thickness validation by 7% in comparison to the use of CMP and default values, and it also substantially improved jet penetration depth and roll formation. Utilizing transient BCs, the shell was validated to be within 10% of BSM. In this particular instance the SS simulation was sufficient in validating shell growth, however it is recommended that the variable BCs be utilized in cases of transient change for better accuracy. A carbon percentage study on F&S shows that the MZ temperature range and TD-Viscosity directly effects flow and therefore shell growth within the mold. Lower carbon steels tend to penetrate deeper and have smaller MZ temperature ranges which increases shell growth because less energy is needed to solidify the shell and the superheat is more evenly distributed in the mold with the deeper penetrating jet.

The VP stress relation more accurately models deformation within the shell in comparison to the PP stress relation because of the addition of the more realistic creep and flow strains. Special attention to the mesh is needed for stress simulations especially near the corners where there is large temperature gradients and also close to the meniscus where the shell is very thin and undergoes excessive bending due to low ferrostatic pressure. Shrinkage of the shell due to thermal contraction requires roughly a 2 to 5mm narrow-face taper for the IC's` thin slab caster depending on the alloy and casting speed. Stress increases in the 40IPM case in comparison to the 20IPM case due to higher temperature gradients near the NF. Results showed that ULCS and lower casting speed require larger mold tapers which was consistent with B.G. Thomas's work. 3D stress analysis shows that mold taper angle, deformation, and stress accumulation is highly dependent on not only the thermal-mechanical MP, but also HT and solidification properties which creates the temperature profile used within the stress simulations. Therefore, higher amounts of localized stress do not necessarily relate to higher amounts of deformation. Deformation or displacement is complex and dependent on multiple contributing factors such as the aforementioned thermal-mechanical MP and temperature gradient, as well as prescribed BCs.

REFERENCES

[1] Birat JP *et al.* (2010) The Making, Shaping and Treating of Steel: Casting Volume. 11th ed. Warrendale: Association for Iron & Steel Technology.

[2] Thomas BG (2018) Intro to Continuous Casting - CCC - U of I. Continuous Casting Consortium.
http://ccc.illinois.edu/introduction/basicphenom.html

[3] "From steel to semi-finished products - tec-science," *tec-science*. [Online]. Available: https://www.tec-science.com/material-science/steel-making/steel-semi-finished-products-continuous-ingot-casting/. [Accessed: 14-Nov-2019].

[4] Thomas BG (2003) Chapter 5 – Modeling of Continuous Casting. In: AISE Steel Foundation, Pittsburg, Pennsylvania

[5] Thomas BG (2005) Modeling of Continuous-Casting Defects Related to Mold Fluid Flow. *AIST - 3rd Internat. Congress on Science & Technology of Steelmaking*, vol. 3, no. 7, pp. 847–861.

[6] Thomas BG (2003) Chapter 14 – Fluid Flow in the Mold. In: AISE Steel Foundation, Pittsburg, Pennsylvania

[7] Seyedein SH, Hasan M (1997) A 3-D Numerical Prediction of Turbulent Flow, Heat Transfer and Solidification in a Continuous Slab Caster for Steel. The Canadian Journal of Metallurgy and Materials Science Vol. 37, Issue 3-4:213-228.

[8] Pfeiler C (2008) Modeling of Turbulent Particle/Gas Dispersion in the Mold Region and Particle Entrapment into the Solid Shell of a Continuous Caster. Ph.D. Thesis, Montanuniversität Leoben

[9] Richmond O, Tien RH (1971) Theory of Thermal Stresses and Air-Gap Formation during the Early Stages of Solidification in a Rectangular Mold. J. Mech. Phys. Solids, 1971, Vol. 19:273-284.

[10] Park JK, Thomas BG, Samarasekera IV (2002) Analysis of thermomechanical behavior in billet casting with different mould corner radii, Ironmaking & Steelmaking, 29:5, 359-375, DOI: 10.1179/030192302225004601

[11] Meng Y, and Thomas BG (2003) Heat-Transfer and Solidification Model of Continuous Slab Casting: CON1D. *Metall. Mater. Trans. B*, vol. 34B, no. October, pp. 685–705.

[12] Thomas BG, Li G, Moitra A, and Habing D (1998) Analysis of thermal and mechanical behavior of copper molds during continuous casting of steel slabs. *80th Steelmak. Conf. Chicago*, pp. 1–19.

[13] Gonzalez M, Goldschmit MB, Assanelli AP, Dvorkin EN, and Berdaguer EF (2003) Modeling of the solidification process in a continuous casting installation for steel slabs. *Metall. Mater. Trans. B*, vol. 34, no. 4, pp. 455–473.

[14] Shamsi MRRI and Ajmani SK (2010) Analysis of mould, spray and radiation zones of continuous billet caster by three-dimensional mathematical model based on a turbulent fluid flow. *Steel Res. Int.*, vol. 81, no. 2, pp. 132–141.

[15] Jiang D and Zhu M (2015) Flow and Solidification in Billet Continuous Casting Machine with Dual Electromagnetic Stirrings of Mold and the Final Solidification. *Steel Res. Int.*, vol. 86, no. 9, pp. 993–1003.

[16] Singh V *et al.* (2016) Modeling of Solidified Shell Formation in Slab Caster and the Role of Process Parameters. in *AISTech 2016 Proceedings* , pp. 1531–1546.

[17] Lopez PER (2020) Advances on Inspection and Numerical Modelling of Surface Defects During Continuous Casting of Steel. TMS 2020 - Defects and Properties of Cast Metal – Continuous Casting Presentation

[18] Metzner AB (1985) Rheology of Suspensions in Polymeric Liquids. J. Rheol. New York, New York. vol. 29, no. 6:739–775

[19] Carman PC (1997) Fluid flow through granular beds, Chem. Eng. Res. Des., vol. 75:S32–S48

[20] Weiner JH, Boley BA (1963) Elasto-Plastic Thermal Stresses in a Solidifying Body. J. Mech Phys. Solids, 1963, Vol 11:145-154

[21] Koric S, Thomas BG (2006) Efficient thermo-mechanical model for solidification processes. Int. J. Numer. Meth. Engng 2006; 66:1955–1989.

[22] Koric S *et al.* (2008) Explicit coupled thermo-mechanical finite element model of steel solidification. Int. J. Numer. Meth. Engng 2009; 78:1–31

[23] Schwerdtfeger K et al. (1998) Stress Formation in Solidifying Bodies. Solidification in a Round Continuous Casting Mold. Metallurgical and Materials Transactions B Volume 29B, Issue 5:1057-1068.

[24] Jay Paidipati et al. (2009) Thin Slab Casing Mould Taper Design. Nucor Steel Design Report.

[25] Li C, Thomas BG (2004) Thermomechanical Finite-Element Model of Shell Behavior in Continuous Casting of Steel. Metallurgical and Materials Transactions Volume 35B:1151-1172.

[26] Zapulla MLS et al. (2019) 3D Thermal-Mechanical Model of Solidifying Steel Strand. Presented at AISTech 2019 — Proceedings of the Iron & Steel Technology Conference 6-9 May 2019. DOI 10.1000.377.224

[27] Takeuchi E and Brimacombe JK (1984) The formation of oscillation marks in the continuous casting of steel slabs. Metallurgical transactions B 15, no. 3: 493-509.

[28] Sengupta, Joydeep, Thomas BG, Shin H, and Kim S (2007) Mechanism of hook formation in ultralow-carbon steel based on microscopy analysis and thermalstress modeling. Iron and Steel Technology 4, no. 7: 83.

[29] Koric S, Thomas BG (2007) Thermo-Mechanical Model of Solidification Processes with Abaqus. Paper presented at 2007 Abaqus Users Conf., May 22-24, 2007

[30] Menter FR (1994) Two-equation eddy-viscosity turbulence models for engineering applications. AIAA J., vol. 32, no. 8:1598–1605

[31] Thomas BG, Stone D (1998) Measurement of Temperature, Solidification, and Microstructure in a Continuous Cast Thin Slab.

[32] LIU Z, LI B, ZHANG L, XU G (2014) Analysis of Transient Transport and Entrapment of particle in Continuous Casting Mold. ISIJ International, vol. 54, No.10:2324-2333

[33] STAR-CCM+™ (2019) User's Manual.

[34] Currey D, Global R, Hamilton D, and Thomas BG (2009) Utilization of CON1D at ArcelorMittal Dofasco ' s No . 2 Continuous Caster for Crater End Determination. *AISTech - Iron Steel Technol. Conf. Proc.*, vol. I, no. 2, pp. 1177–1186.

[35] MatWeb. (2019) AISI 1020 Steel, as Rolled. MatWeb. http://www.matweb.com/search/datasheet.aspx?MatGUID=a2eed65d6e5e4b66b7315a1b30f4b391&ckck=1.